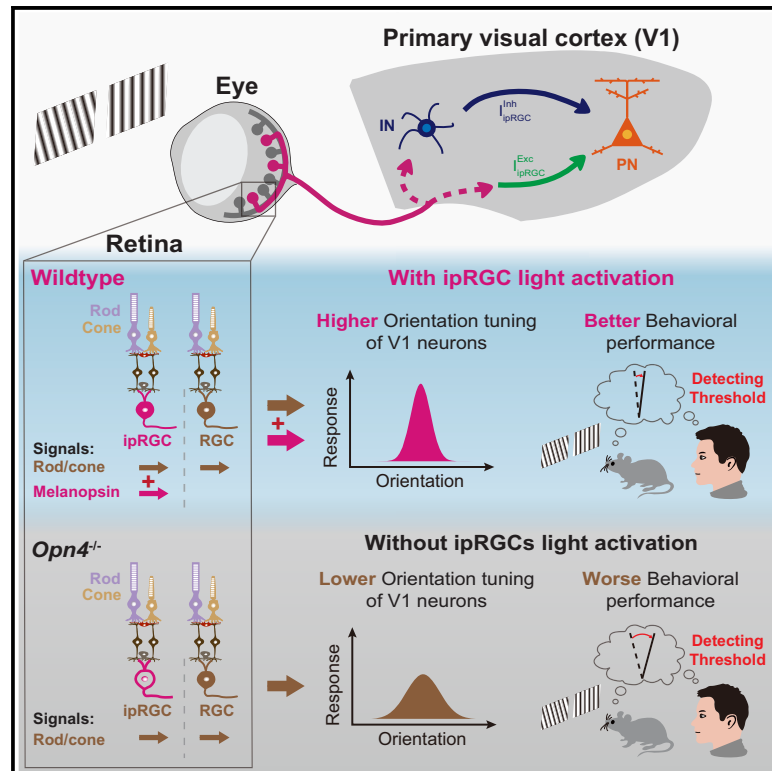


Non-image-forming photoreceptors improve visual orientation selectivity and image perception

Graphical abstract



Authors

Yiming Shi (史逸铭), Jiaming Zhang (张家明), Xingyi Li (李星怡), ..., Zhong Li (李钟), Xiaowei Chen (谌小维), Tian Xue (薛天)

Correspondence

rongliu@ustc.edu.cn (R.L.),
 miyuanyuan@tsinghua.edu.cn (Y.M.),
 jin.bao@siat.ac.cn (J.B.),
 zhongcli@ustc.edu.cn (Z.L.),
 xiaowei_chen@tmmu.edu.cn (X.C.),
 xuetian@ustc.edu.cn (T.X.)

In brief

Using two-photon and multi-channel recordings from mouse primary visual cortex V1, Shi, Zhang, et al. demonstrate that intrinsically photosensitive retinal ganglion cells improve V1 orientation selectivity by differentially modulating excitatory and inhibitory neurons. This modulation by ipRGCs ultimately improves orientation discrimination in both mice and humans.

Highlights

- IpRGCs activation improves mouse V1 L2/3 orientation selectivity
- IpRGCs differently modulate V1 L2/3 excitatory/inhibitory neurons' orientation tuning
- IpRGCs enhance orientation discriminability in mouse and human

Shi et al., 2025, *Neuron* 113, 1–15

February 5, 2025 © 2024 Elsevier Inc. All rights are reserved, including those for text and data mining, AI training, and similar technologies.

<https://doi.org/10.1016/j.neuron.2024.11.015>

Article

Non-image-forming photoreceptors improve visual orientation selectivity and image perception

Yiming Shi (史逸铭),^{1,7} Jiaming Zhang (张家明),^{1,7} Xingyi Li (李星怡),³ Yuchong Han (韩宇崇),¹ Jiangheng Guan (管江衡),² Yilin Li (李祎麟),³ Jiawei Shen (沈嘉伟),¹ Tzvetomir Tzvetanov (赐为),¹ Dongyu Yang (杨栋宇),¹ Xinyi Luo (罗心怡),¹ Yichuan Yao (姚艺川),¹ Zhikun Chu (初治坤),³ Tianyi Wu (伍天一),⁴ Zhiping Chen (陈治平),¹ Ying Miao (苗莹),¹ Yufei Li (李俞霏),¹ Qian Wang (王倩),¹ Jiaxi Hu (胡佳希),¹ Jianjun Meng (孟建军),¹ Xiang Liao (廖祥),² Yifeng Zhou (周逸峰),¹ Louis Tao (陶乐天),⁴ Yuqian Ma (马玉乾),¹ Jutao Chen (陈聚涛),¹ Mei Zhang (章梅),¹ Rong Liu (刘嵘),^{1,*} Yuanyuan Mi (弭元元),^{5,*} Jin Bao (鲍进),^{5,*} Zhong Li (李钟),^{1,*} Xiaowei Chen (谌小维),^{2,*} and Tian Xue (薛天)^{1,8,*}

¹Hefei National Research Center for Physical Sciences at the Microscale, CAS Key Laboratory of Brain Function and Disease, Biomedical Sciences and Health Laboratory of Anhui Province, School of Life Sciences, Division of Life Sciences and Medicine, University of Science and Technology of China, Hefei 230026, China

²Brain Research Center, Third Military Medical University, and Chongqing Institute for Brain and Intelligence, Guangyang Bay Laboratory, Chongqing 400038, China

³Center for Neurointelligence, School of Medicine, Chongqing University, Chongqing 400044, China

⁴Center for Quantitative Biology, Peking University, Beijing 100871, China

⁵Shenzhen Neher Neural Plasticity Laboratory, Shenzhen-Hong Kong Institute of Brain Science-Shenzhen Fundamental Research Institutions, the Key Laboratory of Biomedical Imaging Science and System, Shenzhen Institute of Advanced Technology, Chinese Academy of Sciences, Shenzhen 518055, China

⁶Department of Psychological and Cognitive Sciences, Tsinghua University, Beijing 100084, China

⁷These authors contributed equally

⁸Lead contact

*Correspondence: rongliu@ustc.edu.cn (R.L.), miyuanyuan@tsinghua.edu.cn (Y.M.), jin.bao@siat.ac.cn (J.B.), zhongcli@ustc.edu.cn (Z.L.), xiaowei_chen@tmmu.edu.cn (X.C.), xuetian@ustc.edu.cn (T.X.)

<https://doi.org/10.1016/j.neuron.2024.11.015>

SUMMARY

It has long been a decades-old dogma that image perception is mediated solely by rods and cones, while intrinsically photosensitive retinal ganglion cells (ipRGCs) are responsible only for non-image-forming vision, such as circadian photoentrainment and pupillary light reflexes. Surprisingly, we discovered that ipRGC activation enhances the orientation selectivity of layer 2/3 neurons in the primary visual cortex (V1) of mice by both increasing preferred-orientation responses and narrowing tuning bandwidth. Mechanistically, we found that the tuning properties of V1 excitatory and inhibitory neurons are differentially influenced by ipRGC activation, leading to a reshaping of the excitatory/inhibitory balance that enhances visual cortical orientation selectivity. Furthermore, light activation of ipRGCs improves behavioral orientation discrimination in mice. Importantly, we found that specific activation of ipRGCs in human participants through visual spectrum manipulation significantly enhances visual orientation discriminability. Our study reveals a visual channel originating from “non-image-forming photoreceptors” that facilitates visual orientation feature perception.

INTRODUCTION

Vision is one of the most important human senses. The ability to recognize objects and shapes in images relies on the processing of visual features such as orientation selectivity in the primary visual cortex (V1).^{1–3} All image information originates from retinal photoreceptors and is then conveyed to the visual cortex via the visual thalamus. Other than the classic image-forming photoreceptors, rods and cones, intrinsically photosensitive retinal ganglion cells (ipRGCs) expressing melanopsin as photosensitive protein⁴ have long been considered to mediate non-image-forming functions, such as light-regulated

pupillary constriction,^{5,6} circadian rhythms,^{7,8} mood,^{9–15} development,^{16–23} and metabolism.^{24–26} Previous studies have shown that melanopsin phototransduction enhances the contrast sensitivity of M4 ipRGCs (ON alpha RGCs) in the retina^{27–29} and that ipRGCs contribute rough perception to luminance contrast at the dorsal lateral geniculate nucleus (dLGN),^{30–35} implying a potential role of ipRGCs in contrast detection. However, while image recognition, such as contour and shape discrimination, needs more advanced features extracted at V1, it remains unknown whether ipRGCs influence cortical visual feature processing and further affect mammalian image recognition.

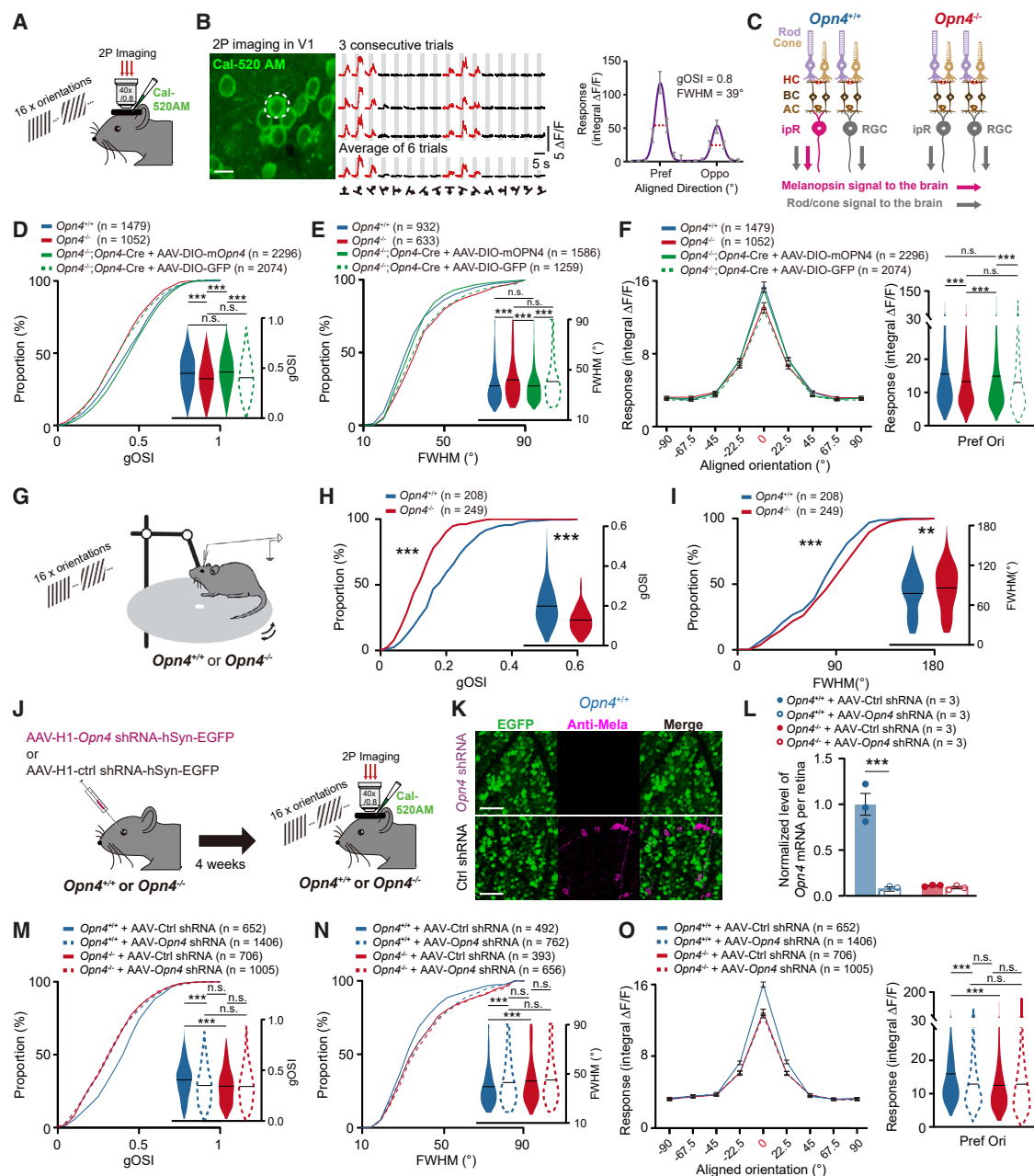


Figure 1. Melanopsin expression is essential for ipRGC-improved orientation selectivity of V1 L2/3 neurons in mice

(A) Schematic diagram of synchronized two-photon Ca^{2+} imaging in V1 of mice while presenting visual stimuli of 16 different orientations. (B) Ca^{2+} responses of a representative V1 L2/3 neuron (dashed circle) to 16-direction drifting gratings. Left: fluorescent image of the Cal-520 AM-loaded field of view. The white dashed circle indicates the representative neuron. Scale bar, 20 μm . Middle: the drifting-grating-evoked Ca^{2+} traces of the representative neuron. The black arrows at the bottom represent moving directions of gratings. Right: orientation tuning curve fitting of the representative neuron. The preferred orientation was aligned to 90° . The dashed red line represents the tuning bandwidth (FWHM). (C) Schematic diagram of retinal structure of $Opn4^{+/+}$ and $Opn4^{-/-}$ mice. In the retina of $Opn4^{+/+}$ mice, ipRGCs transmit both intrinsic signals from melanopsin and signals from rod and cone to brain, while RGCs only transmit signals from rod and cone. In $Opn4^{-/-}$ mice, ipRGCs lack intrinsic photosensitivity and only transmit signals from rods and cones to the brain. HC, horizontal cell; BC, bipolar cell; AC, amacrine cell; RGCs, retinal ganglion cell; ipR, ipRGC. (D) Cumulative frequency (left) and frequency (right) distribution of gOSI of V1 L2/3 neurons from four groups ($Opn4^{+/+}$, $Opn4^{-/-}$, $Opn4^{-/-};Opn4-Cre + AAV-DIO-mOpn4$, and $Opn4^{-/-};Opn4-Cre + AAV-DIO-GFP$). The bars of frequency distribution are presented for the means. Kruskal-Wallis followed by multiple comparisons. (E) Same as (D), but for FWHM. The bars of frequency distribution are presented for the means. Kruskal-Wallis followed by multiple comparisons.

(legend continued on next page)

Here, using *in vivo* two-photon Ca^{2+} imaging, we revealed that light activation of ipRGCs improves the orientation selectivity of V1 layer 2/3 (L2/3) neurons by increasing the neuronal responses at preferred orientations (Pref-Ori) and by sharpening the bandwidth of orientation tuning curves. We further revealed that the light sensation of ipRGCs excites both excitatory pyramidal neurons and inhibitory interneurons in V1 L2/3 and differentially influences their tuning properties, leading to a reshaping of the cortical excitatory and inhibitory balance to improve visual feature processing. Behavioral tests demonstrated that the activation of ipRGCs indeed improves the orientation discriminability in mice. Furthermore, we revealed that ipRGCs' activity improves the resilience of orientation selectivity under the interference of image noise. Importantly, we demonstrated that in human participants, specific activation of ipRGCs by visual spectrum manipulation significantly enhances the discrimination to visual orientations. Our work unveils an image-forming visual channel originating from non-image-forming photoreceptors that improves cortical feature processing, revising the dogma for decades that image contour perception was only mediated by rods and cones, and highlights the impact of the melanopsin-sensitive spectrum to the optimization of light conditions for working and life.

RESULTS

Activation of ipRGCs improves the orientation selectivity of V1 L2/3 neurons in mouse

To investigate the contribution of ipRGCs to visual cortical orientation selectivity, we employed *in vivo* two-photon Ca^{2+} imaging to record the responses of mouse V1 L2/3 neurons loaded with the Ca^{2+} indicator Cal-520 AM^{36,37} to visual stimuli of drifting gratings in 16 directions. The global orientation selective index (gOSI) and tuning bandwidth (defined as the full width at half maximum of the tuning curve, FWHM) were measured by the drifting-grating-evoked Ca^{2+} responses to characterize the V1 orientation selectivity (Figures 1A and 1B; see STAR Methods). Higher gOSI values and narrower FWHM indicate enhanced orientation selectivity. Melanopsin, the photosensitive protein

expressed in the membranes of ipRGCs, is encoded by the *Opn4* gene. To assess the role of ipRGCs, we compared the orientation selectivity of V1 neurons in *Opn4*^{-/-} mice, a knockout line lacking the *Opn4* gene, with their wild-type littermates (*Opn4*^{+/+}) (Figure 1C). The results showed that the V1 L2/3 neurons of *Opn4*^{-/-} mice exhibited significantly reduced gOSI and broader FWHM compared with wild-type controls (Figures 1D and 1E). The multi-channel extracellular electrophysiological recording further corroborated this observation at the level of neuronal spiking activity (Figures 1G–1I). The observed decrease in the gOSI was primarily attributed to diminished Ca^{2+} responses at Pref-Ori (Figure 1F) rather than alterations in responses at orthogonal orientations (Orth-Ori response) (Figure S1B). There were no significant differences in the percentage of responsive neurons between wild-type and *Opn4*^{-/-} mice V1 or in neuronal response variability (Figures S1A and S1C), suggesting that cortical response variability was unaffected by ipRGC input. Furthermore, the orientation selectivity of V1 neurons is suggested to be associated with the shape of the receptive field (RF), as the elongation of the RF is closely associated with orientation selectivity.^{38–43} To investigate whether ipRGCs alter the shape of the V1 RF, we employed multi-channel spiking recordings synchronized with a “locally sparse noise” visual stimulus³⁹ to delineate the spatial RFs of V1 neurons (Figures S1D and S1E). We calculated the short/long axis ratio to quantify the elongation of ON/OFF subdomains. A smaller short/long axis ratio indicates that the ON/OFF subdomain is more elongated. Our results indicated that compared with wild-type mice, V1 neurons in *Opn4*^{-/-} mice exhibited a significantly larger short/long axis ratio of ON/OFF subdomains (Figures S1F₁ and S1G₁), suggesting that *Opn4*^{-/-} mice show more isotropic RFs in V1. This difference is consistent within V1 simple cells (Figures S1F₂–S1G₂). Above all, these results suggest an impairment in orientation selectivity in the V1 of *Opn4*^{-/-} mice.

To rule out the potential developmental and genetic background interference,²² we first restored the melanopsin expression in ipRGCs of adult *Opn4*^{-/-}; *Opn4*-Cre mice using AAV-DIO-m*Opn4*-EGFP intravitreal injection (rescued group), while

(F) Left: mean response at each of 8 orientations of V1 L2/3 neurons from the four groups in (D). The preferred orientations of each cell were aligned to 90°. Data are mean ± SEM. Right: the distribution of V1 L2/3 neuronal responses to preferred orientations from the four groups in (D). The bars of frequency distribution are presented for the means. Kruskal-Wallis followed by multiple comparisons.

(G) Schematic illustration of *in vivo* multi-channel electrophysiological recording in mouse V1 while presenting visual stimuli of 16 different orientations.

(H) Cumulative frequency distribution of gOSIs measured by spikes of responsive V1 L2/3 neurons from *Opn4*^{+/+} and *Opn4*^{-/-} mice. Kolmogorov-Smirnov test. Insets represent frequency distribution. The bars of frequency distribution are presented for the means. Rank-sum test.

(I) Same as (H), but for FWHM. Kolmogorov-Smirnov test. Insets represent frequency distribution. The bars of frequency distribution are presented for the means. Rank-sum test.

(J) Schematic diagram of *Opn4* or control shRNA expression in all types of RGCs of *Opn4*^{+/+} or *Opn4*^{-/-} mice by AAV2/2-H1-*Opn4* shRNA-hSyn-EGFP or AAV2/2-H1-ffLuciferase shRNA-hSyn-EGFP.

(K) Anti-melanopsin immunostaining at RGCs from *Opn4*^{+/+} mice intravitreally injected with AAV-*Opn4* shRNA or AAV-control shRNA. Scale bar, 50 μm.

(L) Real-time PCR of *Opn4* mRNA from the retinas of four groups (*Opn4*^{+/+}/AAV-*Opn4* shRNA, *Opn4*^{+/+}/AAV-control shRNA, *Opn4*^{-/-}/AAV-*Opn4* shRNA, *Opn4*^{-/-}/AAV-control shRNA). Data are mean ± SEM. Two-way ANOVA followed by multiple comparisons.

(M) Cumulative frequency (left) and frequency (right) distribution of gOSIs of V1 L2/3 neurons from the four groups in (L). The bars of frequency distribution are presented for the means. Two-way ANOVA followed by multiple comparisons.

(N) Same as (M), but for FWHM. The bars of frequency distribution are presented for the means. Two-way ANOVA followed by multiple comparisons.

(O) Left: mean response at each of 8 orientations of V1 L2/3 neurons from the four groups in (K). The preferred orientations of each cell were aligned to 90°. Data are mean ± SEM. Right: the distribution of V1 L2/3 neuronal responses to preferred orientations from the four groups in (K). The bars are presented for the means. Two-way ANOVA followed by multiple comparisons.

p* < 0.05, *p* < 0.01, ****p* < 0.001; n.s., no significant difference. See Table S2 for results of statistics.

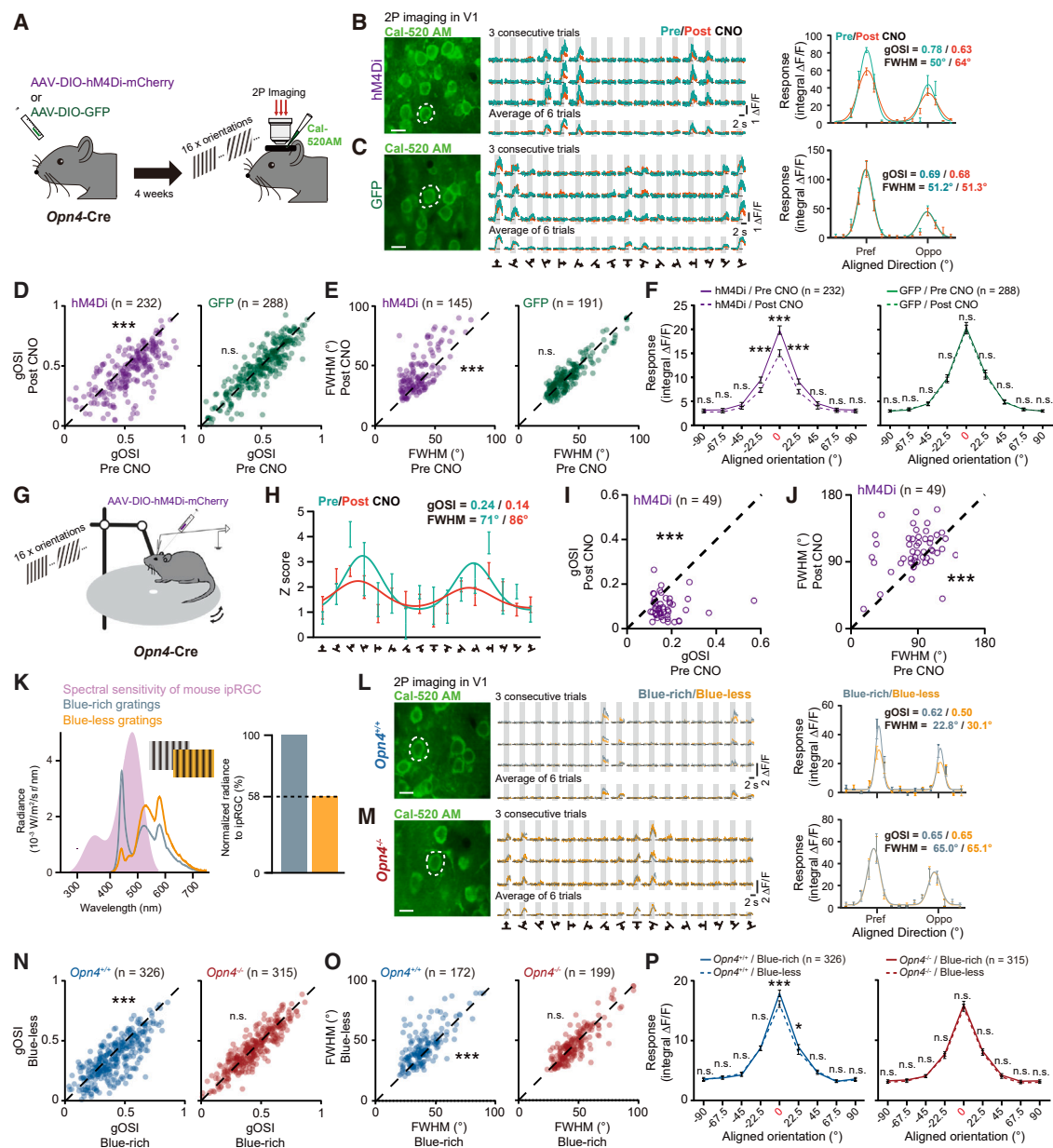


Figure 2. Acute manipulation of ipRGC activity modulates the orientation selectivity of V1 L2/3 neurons in mice

(A) Schematic diagram of hM4Di or GFP expression in ipRGCs of *Opn4*-Cre mice by AAV-DIO-hM4Di-mCherry or AAV-DIO-GFP.

(B and C) Responses and tuning curve fitting of two representative neurons (dashed circles) in V1 L2/3 of hM4Di-expressing (B) and GFP-expressing (C) mice before and after CNO treatment. Data are mean \pm SEM. Scale bar, 20 μ m.

(D) Population summary of CNO-mediated changes in gOSIs of V1 L2/3 neurons in hM4Di-expressing and GFP-expressing mice. Each dot represents one cell. Signed-rank test.

(E) Same as (D), but for FWHM. Each dot represents one cell. Signed-rank test.

(F) The drifting grating-evoked responses to different orientations of the V1 L2/3 neurons in hM4Di-expressing and GFP-expressing mice before and after CNO treatment. The preferred orientations of each cell were aligned to 90°. Data are mean \pm SEM. Signed-rank test.

(G) Schematic illustration of *in vivo* multi-channel electrophysiological recording during orientation stimuli and retinotopic mapping in V1 of *Opn4*-Cre mice injected intravitreally with AAV-DIO-hM4Di-mCherry.

(H) Responses and tuning curve fitting of a representative neuron in V1 L2/3 of hM4Di-expressing mice before and after CNO treatment. Data are mean \pm SEM.

(I) The distribution of gOSIs of V1 of *Opn4*-Cre mice injected intravitreally with AAV-DIO-hM4Di-mCherry measured by spike recording.

(J) Same as (I), but for FWHM.

(K) The spectral radiance distribution of blue-rich and blue-less gratings and the normalized spectral sensitivity of mouse ipRGCs (left). The effective radiance to activate ipRGCs of blue-less gratings is 58% normalized to that of blue-rich gratings (right). The mean luminance of two gratings are matched.

(legend continued on next page)

AAV-DIO-GFP was injected as control (control group) (Figure S1H). Successful restore of melanopsin expression was confirmed by anti-melanopsin immunostaining and the ipRGC-like light responses recorded on EGFP-positive cells (Figure S1I). The two-photon Ca^{2+} imaging was performed 4 weeks later, and the results showed that compared with the control group, mice in the rescued group had larger gOSI and Pref-Ori responses as well as narrower FWHM for V1 L2/3 neurons (Figures 1D–1F), suggesting that restoring melanopsin expression in the ipRGCs significantly improved the V1 orientation selectivity of *Opn4*^{-/-}; *Opn4*-Cre mice. The Orth-Ori responses, as well as the neuronal response variability, did not change between the two groups (Figures S1B and S1C). Furthermore, we used short hairpin RNAs (shRNAs) to knock down *Opn4* mRNA expression in adult mouse retina.⁴⁴ Specifically, we injected AAV2/2-H1-*Opn4* shRNA-hSyn-EGFP into the eyes of adult wild-type mice to knock down *Opn4* mRNA expression or AAV2/2-H1-*ffLuciferase* shRNA-hSyn-EGFP as a control (Figure 1J). In the retinas of wild-type mice expressing *Opn4* shRNA, anti-melanopsin immunostaining showed no detectable fluorescent signal, and real-time PCR results showed a significant decrease in the expression level of *Opn4* mRNA, while the retinas expressing control shRNA had normal anti-melanopsin signals and *Opn4* mRNA expression levels (Figures 1K and 1L). We then recorded the drifting grating-evoked Ca^{2+} responses of V1 L2/3 neurons from these mice. The results showed that *Opn4* shRNA induced a significant decrease in the gOSI and Pref-Ori response and an increase in FWHM of V1 L2/3 neurons in wild-type mice (Figures 1M–1O), but it did not alter the Orth-Ori response or the neuronal response variability (Figures S1K and S1L). Importantly, *Opn4* shRNA expression in *Opn4*^{-/-} retinas (Figure S1J) did not significantly change the gOSI, Pref-Ori response, or FWHM in mouse V1 (Figures 1M–1O), indicating that the *Opn4* shRNA does not have any non-specific effects. Overall, these results suggest that melanopsin expression, which is responsible for the intrinsic photoactivation of ipRGCs, is necessary for improving V1 orientation selectivity.

We next investigated whether the activity of ipRGCs modulates V1 orientation selectivity. First, we applied a chemogenetic tool to acutely reduce the activity of ipRGCs when presented with orientation stimuli. Specifically, we used AAV-DIO-hM4Di-mCherry to express hM4Di receptors in the ipRGCs of *Opn4*-Cre mice (hM4Di-expressing group), while the control group was injected with AAV-DIO-GFP (GFP-expressing group) (Figure 2A). The success of hM4Di expression in ipRGCs was demonstrated by the decreases in light-evoked ipRGCs' spike frequencies and pupillary constriction after clozapine-N-oxide (CNO) application (Figures S2A–S2C). Two-photon Ca^{2+} imaging

was performed 4 weeks later, and the same population of V1 L2/3 neurons was recorded both before and after intraperitoneal injection of CNO. The results showed that after CNO injection, V1 L2/3 neurons in hM4Di-expressing mice exhibited reduced gOSI, smaller Pref-Ori response, and broader FWHM, whereas these properties of orientation selectivity were not altered in the control GFP-expressing group (Figures 2B–2F). The Orth-Ori responses and neuronal response variability were not altered by CNO application in either group (Figures 2F and S2H). Furthermore, multi-channel spiking recording also revealed that after CNO injection, V1 L2/3 neurons in hM4Di-expressing mice exhibited decreased gOSI, increased FWHM, and less elongated ON/OFF subdomains (Figures 2G–2J and S2D–S2G). These results indicate that the reduction in neuronal activity of ipRGCs impairs mouse V1 L2/3 orientation selectivity.

To further investigate whether the light activation of ipRGCs contributes to the improvement of cortical orientation selectivity, we altered the visual spectrum to generate “blue-less” gratings, which have 58% efficiency for melanopsin activation but have the same mean luminance as “blue-rich” gratings (Figure 2K), and then presented them to wild-type and *Opn4*^{-/-} mice. The two-photon Ca^{2+} imaging results showed that compared with blue-rich gratings, blue-less gratings significantly decrease gOSI and Pref-Ori responses and increase FWHM in the V1 L2/3 of wild-type mice (Figures 2L–2P). These differences were absent in V1 L2/3 of *Opn4*^{-/-} mice (Figures 2L–2P). The Orth-Ori responses and neuronal response variability were also not altered within the two groups (Figures 2P and S2I). Notably, the statistical differences in the gOSI and FWHM remained consistent when analyzed by averaging within animals or across fields of view (FOVs) in each experiment (Figures S1M–S1P and S2J–S2M). Overall, these results demonstrate that the activation of ipRGCs improves orientation selectivity at the visual cortex.

Light sensation of ipRGCs alone is sufficient to activate both V1 L2/3 excitatory and inhibitory neurons

To test whether there is a functional connection between ipRGCs and V1, we performed two-photon Ca^{2+} imaging of V1 L2/3 neurons in *rd1;cDTA* (melanopsin-only, MO) mice, in which all rods and cones degenerate in adulthood, leaving melanopsin-expressing ipRGCs as the only photoreceptors in the retina (Figure 3A). We presented blue light illumination (7.35×10^{16} photons/cm²/s, 470 nm, 20 s) to the eyes of MO mice and observed Ca^{2+} responses in an average of 21% of V1 L2/3 neurons (Figures 3B and S3C). Two-photon Ca^{2+} imaging-guided *in vivo* loose-patch recording revealed that light-induced Ca^{2+} rises in the V1 L2/3 of MO mice corresponded to an increase in spike frequencies (Figures S3A and S3B). These light-induced Ca^{2+} responses

(L and M) Responses and tuning curve fitting of two representative neurons (dashed circles) in the V1 L2/3 of *Opn4*^{+/+} (L) and *Opn4*^{-/-} (M) mice to blue-rich and blue-less drifting gratings. Data are mean \pm SEM. Scale bar, 20 μ m.

(N) Population summary of spectra-mediated changes in gOSIs of the V1 L2/3 of *Opn4*^{+/+} and *Opn4*^{-/-} mice. Each dot represents one cell. Signed-rank test.

(O) Same as (N), but for FWHM. Each dot represents one cell. Signed-rank test.

(P) The grating-evoked responses to different orientations of the V1 L2/3 of *Opn4*^{+/+} and *Opn4*^{-/-} mice. The preferred orientations of each cell were aligned to 90°. Data are mean \pm SEM. Signed-rank test.

* $p < 0.05$, ** $p < 0.01$, *** $p < 0.001$; n.s., no significant difference. See Table S2 for results of statistics.

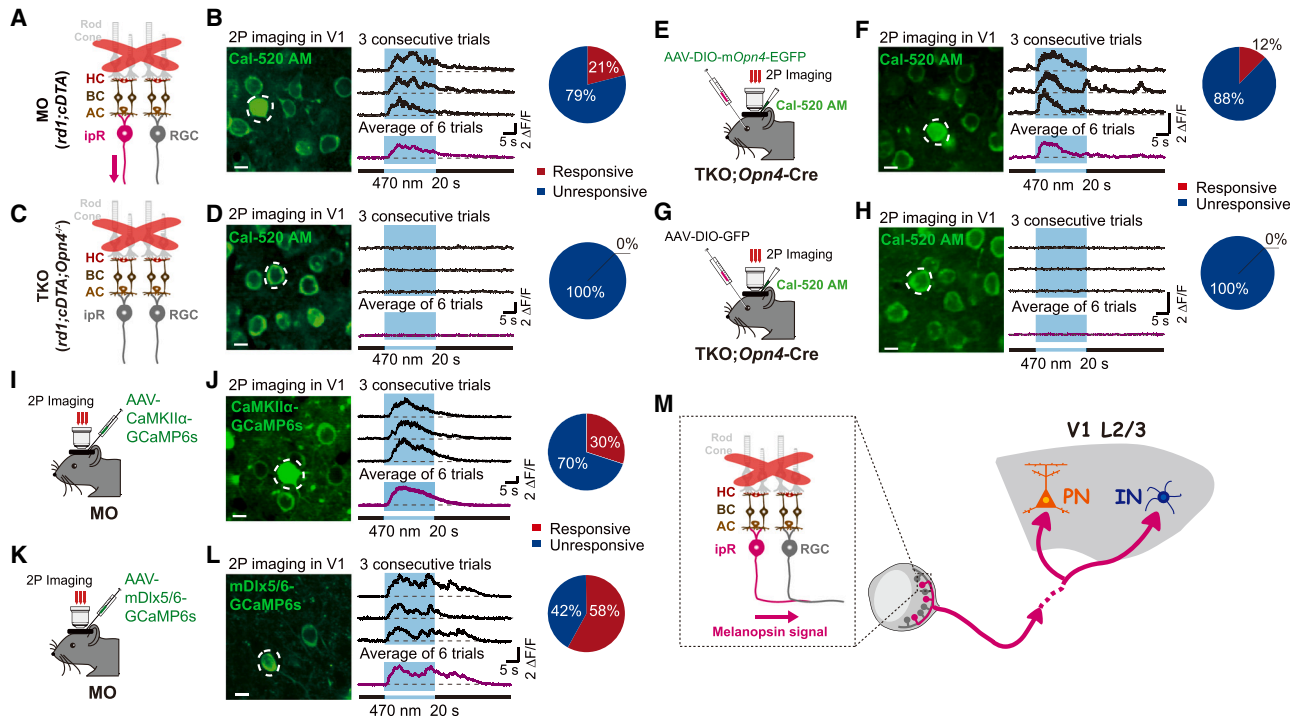


Figure 3. ipRGCs transmit melanopsin-dependent light signals to activate both excitatory and inhibitory V1 L2/3 cortical neurons

(A) Schematic illustration of a melanopsin-only mouse (MO, *rd1;cDTA*) retina with degenerated rods and cones but intact ipRGCs.
 (B) Ca^{2+} responses of a representative neuron (dashed circle) in response to a 20-s blue light stimulus in MO mouse V1 L2/3. The pie chart (right) shows that, on average, 21% of V1 L2/3 neurons responded to blue light. Light intensity was 7.35×10^{16} photons/cm²/s. Scale bar, 10 μm .
 (C) Schematic illustration of a triple knockout (TKO, *rd1;cDTA;Opn4^{-/-}*) retina with degenerated rods and cones and nonphotoreceptive ipRGCs.
 (D) No Ca^{2+} response was detected in a representative focal plane from TKO mouse V1 L2/3. The pie chart (right) shows that no V1 L2/3 neuron responded to blue light. Light intensity was 7.35×10^{16} photons/cm²/s. Scale bar, 10 μm .
 (E) Schematic diagram of melanopsin expression in ipRGCs of TKO;*Opn4-Cre* mice by AAV-DIO-*mOpn4-EGFP* intravitreal injection.
 (F) Ca^{2+} responses of a representative V1 L2/3 neuron in TKO;*Opn4-Cre* mice intravitreally injected with AAV-DIO-*mOpn4-EGFP*. The pie chart (right) shows that, on average, 12% of V1 L2/3 neurons responded to blue light. Scale bar, 10 μm .
 (G) Schematic diagram of GFP expression in ipRGCs of TKO;*Opn4-Cre* mice by AAV-DIO-GFP intravitreal injection.
 (H) Ca^{2+} response of a representative V1 L2/3 neuron in TKO;*Opn4-Cre* mice intravitreally injected with AAV-DIO-GFP. The pie chart (right) shows that no V1 L2/3 neuron responded to blue light. Scale bar, 10 μm .
 (I) Schematic diagram of AAV-CaMKII α -GCaMP6s expression of V1 L2/3 excitatory neurons in MO mice.
 (J) Ca^{2+} response of a representative V1 L2/3 neuron expressing CaMKII α -GCaMP6s of MO mouse (left). The pie chart (right) shows that, on average, 30% of GCaMP6s-labeled V1 L2/3 neurons responded to blue light. Scale bar, 10 μm .
 (K) Schematic diagram of AAV-mDlx5/6-GCaMP6s expression of V1 L2/3 interneurons in MO mice.
 (L) Ca^{2+} response of an example V1 L2/3 neuron expressing mDlx5/6-GCaMP6s of MO mouse (left). The pie chart (right) shows that, on average, 58% of GCaMP6s-labeled V1 L2/3 neurons responded to blue light. Scale bar, 10 μm .
 (M) Schematic diagram illustrates that light sensation of ipRGC activates both V1 excitatory pyramidal neurons and inhibitory interneurons. PN, excitatory pyramidal neuron; IN, inhibitory interneuron.

* $p < 0.05$, ** $p < 0.01$, *** $p < 0.001$; n.s., no significant difference. See Table S2 for results of statistics.

were abolished in *rd1;cDTA;Opn4^{-/-}* (triple knockout, TKO) mice, which were eliminated of rods, cones, and melanopsin (Figures 3C and 3D), suggesting that the light-induced responses in the V1 of MO mice are ipRGC-photoreception dependent. The light-induced Ca^{2+} responses in MO mouse V1 were light-intensity dependent, as brighter light induced faster onsets and larger amplitudes of Ca^{2+} responses, as well as increased the number of responsive neurons (Figures S3E–S3H). Restoring melanopsin expression in ipRGCs rescued the light responsiveness of the V1 in *rd1;cDTA;Opn4^{-/-};Opn4-Cre* (TKO;*Opn4-Cre*) adult mice (Figures 3E and S3I), with 12% of V1 L2/3 neurons showing light-induced Ca^{2+} responses in TKO;*Opn4-Cre* mice (Figures 3F and

S3D), while no such response was detected in TKO;*Opn4-Cre* mice injected with a GFP-only-expressing AAV as a control (Figures 3G, 3H, and S3D).

Since V1 L2/3 orientation selectivity is functionally attributed to the total excitatory and inhibitory inputs,^{42,45–48} we next identified the types of V1 neurons that were activated by ipRGCs. To this purpose, we injected AAV-CaMKII α -GCaMP6s or AAV-mDlx5/6-GCaMP6s into the V1 of MO mice to label excitatory or inhibitory neurons, respectively (Figures 3I and 3K). Indeed, post hoc immunostaining showed that 94.2% of CaMKII α -GCaMP6s-positive and 92.8% of mDlx5/6-GCaMP6s-positive neurons were glutamate or GABA positive (Figures S3J

and S3K). On average, 30% and 58% of CaMKII α - and mDlx5/6-GCaMP6s-positive neurons, respectively, in MO mice V1 L2/3 were activated by light (Figures 3J and 3L). These results demonstrate that ipRGCs transmit melanopsin-dependent light signals to excite both excitatory and inhibitory V1 L2/3 cortical neurons (Figure 3M).

Differential influence of ipRGCs to the tuning properties of cortical excitatory and inhibitory neurons improves V1 orientation selectivity

To investigate ipRGCs' contribution to the tuning properties of V1 excitatory neurons and inhibitory interneurons, we recorded the Ca²⁺ response of CaMKII α - or mDlx5/6-GCaMP6s-labeled neurons in the V1 L2/3 of wild-type and *Opn4*^{-/-} mice when the orientation stimuli were presented (Figures 4A and 4E). The two-photon Ca²⁺ imaging results showed that V1 L2/3 excitatory neurons had statistically significant larger gOSIs, increased Pref-Ori responses, and narrower FWHM in wild-type mice compared with *Opn4*^{-/-} mice (Figures 4B–4D), while the Orth-Ori responses were not changed between the two groups (Figure 4C), consistent with the result revealed by experiments with neurons loaded by Cal-520 AM. Meanwhile, V1 L2/3 inhibitory interneurons in wild-type mice had significantly larger Ca²⁺ responses for all orientations (Figure 4G) and lower gOSIs (Figure 4F) compared with *Opn4*^{-/-} mice, while FWHM showed no difference (Figure 4H), suggesting that the light sensation of ipRGCs activates V1 L2/3 inhibitory interneurons in a broadly tuned manner. The differences in gOSIs and FWHM also remained consistent when analyzed by averaging within animals or across FOVs (Figures S4A–S4D). The neuronal response variability of V1 excitatory and inhibitory neurons had no significant difference between wild-type and *Opn4*^{-/-} mice (Figures S4E and S4F).

To explain how ipRGC-mediated inputs alter V1 tuning properties, we built a continuous attractor neural network (CANN, Figure 4I) to model V1 L2/3 excitatory neuron orientation tuning.⁴⁹ Inputs to the CANN included the original basal inputs (I_{RGC}) and additional ipRGC-driven excitatory (I_{ipRGC}^{Exc}) and inhibitory (I_{ipRGC}^{Inh}) inputs (Figure 4J). The model demonstrated that I_{ipRGC}^{Exc} to the CANN increased neuronal responses at the Pref-Ori and that I_{ipRGC}^{Inh} sharpened neuronal orientation tuning (Figures 4K, 4L, and S4G–S4J), which is consistent with our experimental data (Figure 1) and suggests that ipRGCs' light activation drives excitatory and inhibitory inputs to V1 L2/3 to jointly improve V1 orientation selectivity (Figure 4M). These results reveal that ipRGCs activation differentially influences V1 excitatory and inhibitory neurons, which consequently reshape the cortical excitatory and inhibitory balance to improve orientation selectivity.

Light activation of ipRGCs behaviorally improves orientation discriminability in mouse

To investigate the effect of ipRGCs on image visual perception behaviorally, we applied a series of Go/No-Go tasks to mice to measure the orientation discriminability.⁴⁸ For each task, the Go stimulus consists of drifting gratings with orientations of 90° (vertical), while the gratings of the No-Go stimulus are θ° away from that of the Go stimulus (e.g., in the $\Delta 30^\circ$ task, the orientation of No-Go stimulus is 60°) (Figure 5A). Mice were first

trained by two easy tasks ($\Delta 60^\circ$ and 45°) and then tested by 6 hard tasks ($\Delta 30^\circ$, 25° , 20° , 15° , 12° , and 10°) to get the orientation discrimination index (d') for each orientation difference (Figures 5B, 5C, S5A, and S5B). For context, higher d' values (calculated from the hit rate and false alarm rate in a single session, see STAR Methods) indicate a higher ability to discriminate two different orientations; by fitting the measured d' values to the corresponding orientation differences by the Sigmoid function, we obtained the discrimination threshold (defined as fitted d' value = 1) for each mouse (Figure 5C; see STAR Methods). We found that wild-type mice had a significantly better discriminability for small orientation differences ($\Delta 15^\circ$, 12° , and 10°) compared with *Opn4*^{-/-} littermates, as wild-type mice exhibited larger d' in tasks with small orientation differences and lower discrimination thresholds (Figures 5E and 5F). Restoring melanopsin expression in the ipRGCs of *Opn4*^{-/-}; *Opn4*-Cre mice (Figure 5G) significantly improved orientation discriminability, but there was no difference in GFP-expressing control mice (Figures 5H and 5I).

We further applied blue-rich and blue-less gratings in the Go/No-Go task with a small orientation difference ($\Delta 10^\circ$ task) (Figure 5J). Wild-type mice had significantly better discriminability in the $\Delta 10^\circ$ task when presented with blue-rich gratings instead of blue-less gratings, whereas no significant difference was observed in *Opn4*^{-/-} mice (Figure 5K). Restoring melanopsin expression in ipRGCs of *Opn4*^{-/-}; *Opn4*-Cre mice also significantly improved the orientation discriminability to blue-rich gratings compared with blue-less gratings, while no difference was observed in GFP-expressing control mice (Figures 5L and 5M). These results demonstrated that the light activation of ipRGCs improves orientation discriminability in mice.

Cortical inputs from ipRGCs enhance the resilience to external visual noise

Since the visual scene in realistic environments consists of target features as well as background interference, we investigated the contribution of ipRGCs to the visual feature extraction embedded in white and black visual noises in various contrasts. We generated drifting gratings in 30% Michelson contrast and alternatively overlapped them with black-and-white noise in different contrast ranges (30%, 50%, and 70%, Figure 5N). We recorded the V1 L2/3 neuronal responses of wild-type and *Opn4*^{-/-} mice and employed the population vector method (i.e., a linear decoder) to decode and compare the orientation representation accuracies under various visual noise scenarios between wild-type and *Opn4*^{-/-} mice. The population vector infers the orientation by computing the mean of neurons' preferred directions weighted by their responses. The decoding result for each visual orientation (θ_m^β) presented in the m th trial at a given visual noise strength (β) is denoted as $\theta_m^{\beta, decoded}$. We assessed the representational accuracy in the m th trial by calculating the representation bias $P_m^{\beta, bias} = |\theta_m^{\beta, decoded} - \theta_m^\beta|$ (Figure 5O), and the final results were obtained by averaging across all trials and animals. Our results indicated that (1) at the same noise strength, wild-type mice consistently outperformed *Opn4*^{-/-} mice in representational accuracy, with statistical significance and (2) the difference in discrimination biases between wild-type and

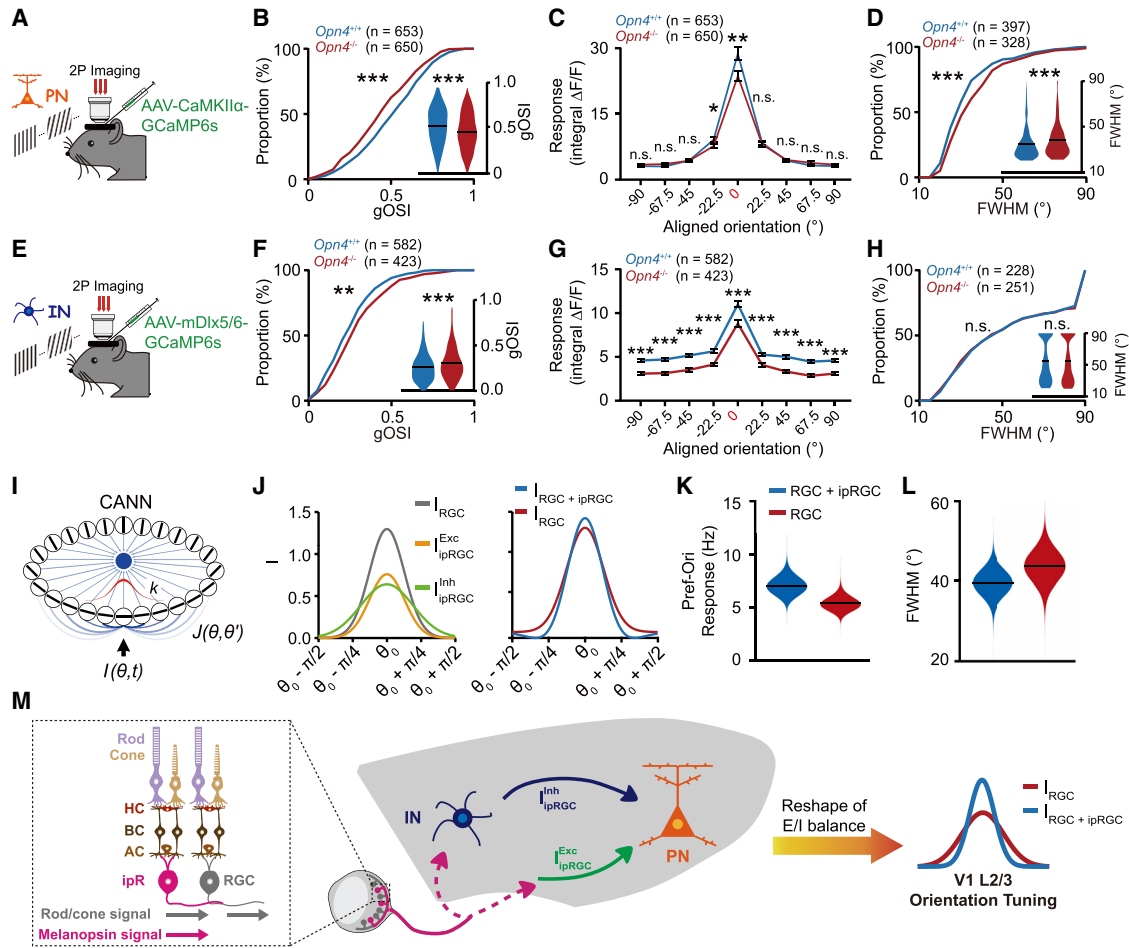


Figure 4. Light activation of ipRGCs reshapes cortical excitatory and inhibitory balance to improve orientation selectivity

(A) Schematic diagram of a Ca^{2+} recording of V1 L2/3 excitatory neurons in $\text{Opn4}^{+/+}$ and $\text{Opn4}^{-/-}$ mice.

(B) Cumulative frequency distribution of gOSIs of responsive V1 L2/3 excitatory neurons from $\text{Opn4}^{+/+}$ and $\text{Opn4}^{-/-}$ mice. Kolmogorov-Smirnov test. Insets represent frequency distribution. The bars of frequency distribution are presented for the means. Rank-sum test.

(C) Mean response at each of 8 orientations of responsive V1 L2/3 excitatory neurons from $\text{Opn4}^{+/+}$ and $\text{Opn4}^{-/-}$ mice. The preferred orientations of each cell were aligned to 90° . Data are mean \pm SEM. Rank-sum test.

(D) Same as (B), but for FWHM. Kolmogorov-Smirnov test. Insets represent frequency distribution. The bars of frequency distribution are presented for the means. Rank-sum test.

(E) Schematic diagram of Ca^{2+} recording of V1 L2/3 interneurons in $\text{Opn4}^{+/+}$ and $\text{Opn4}^{-/-}$ mice.

(F) Cumulative frequency distribution of gOSIs of responsive V1 L2/3 interneurons from $\text{Opn4}^{+/+}$ and $\text{Opn4}^{-/-}$ mice. Kolmogorov-Smirnov test. Insets represent frequency distribution. The bars of frequency distribution are presented for the means. Rank-sum test.

(G) Mean response at each of 8 orientations of responsive V1 L2/3 interneurons from $\text{Opn4}^{+/+}$ and $\text{Opn4}^{-/-}$ mice. The preferred orientations of each cell were aligned to 90° . Data are mean \pm SEM. Rank-sum test.

(H) Same as (F), but for FWHM. Kolmogorov-Smirnov test. Insets represent frequency distribution. The bars of frequency distribution are presented for the means. Rank-sum test.

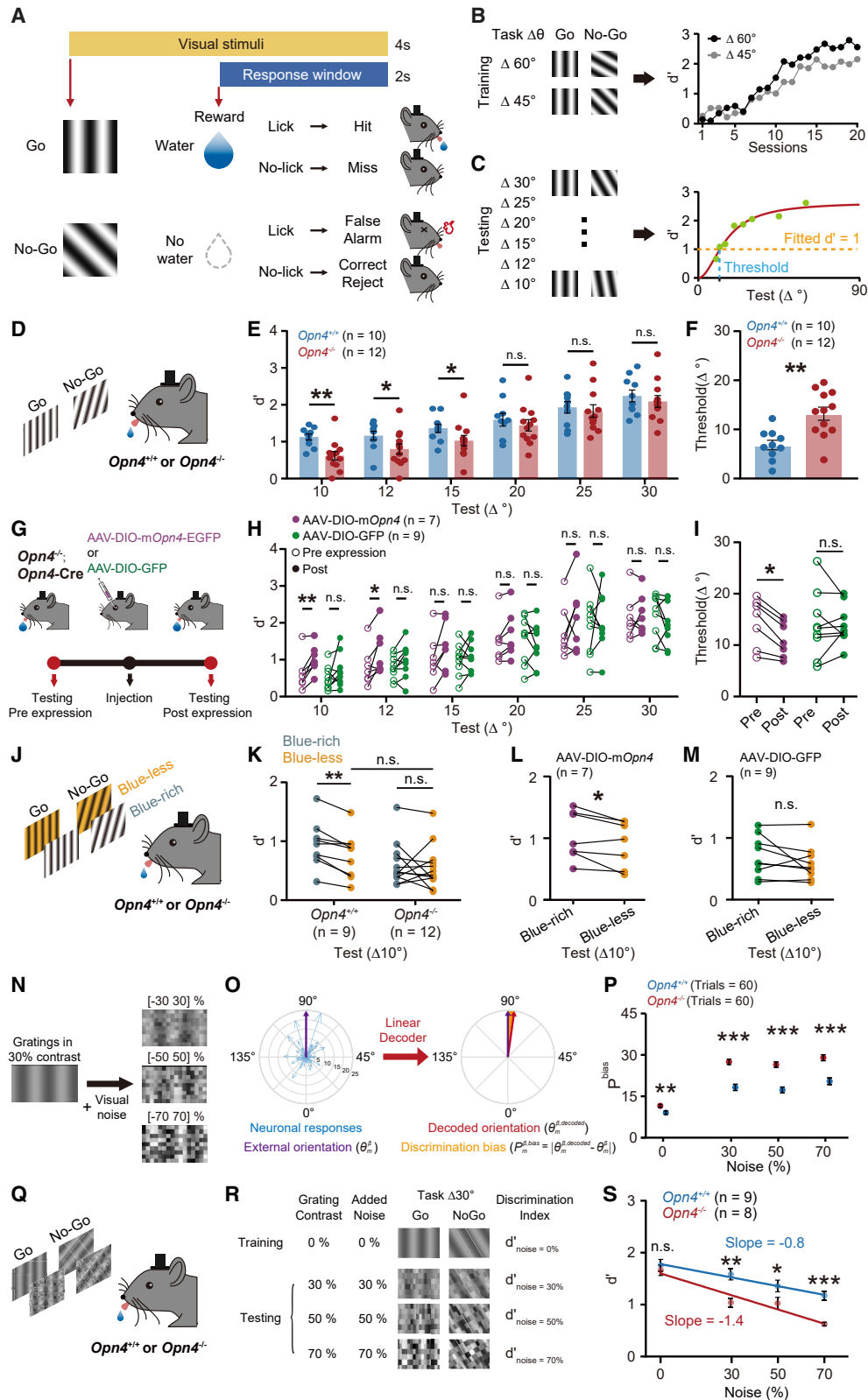
(I) The structure of the CANN. Excitatory neurons are aligned on a ring according to their preferred orientations $\theta \in (-\pi/2, +\pi/2]$ and are connected in a translation-invariant manner in the form of $J(\theta, \theta')$. The inhibitory effect is modeled by divisive normalization, with k controlling the global inhibition strength (the gray lines). In response to an external input signal ($I_{\text{ext}}(\theta, t)$), the CANN generates a Gaussian-shaped bump (red curve) at the corresponding stimulus location.

(J) Left: original basal inputs (I_{RGC}) and additional ipRGC-mediated excitatory ($I_{\text{ipRGC}}^{\text{Exc}}$) and inhibitory ($I_{\text{ipRGC}}^{\text{Inh}}$) inputs. Right: total external inputs driven by ipRGCs, where the excitatory and inhibitory parts are balanced ($\alpha^E = 1.5, \alpha_{\text{ipRGC}}^E = 0.7, \alpha_{\text{ipRGC}}^I = 0.5$), sharpen the orientation tuning.

(K and L) Simulation results. The Pref-Ori responses increase, and FWHMs of the tuning curves decrease, due to the contribution of ipRGC inputs. The bars are presented for the means.

(M) The ipRGC-induced cortical excitatory and inhibitory inputs to pyramidal neurons change the cortical excitatory and inhibitory (E/I) balance and consequently sharpen the orientation tuning in V1 L2/3.

* $p < 0.05$, ** $p < 0.01$, *** $p < 0.001$; n.s., no significant difference. See Table S2 for results of statistics.



(legend on next page)

Opn4^{-/-} mice is larger when stimuli are disrupted by external noise (Figure 5P). This result indicates that cortical inputs from ipRGCs enhance V1 resilience to external visual noise.

We further tested the ipRGC-enhanced V1 resilience to external visual noise behaviorally (Figure 5Q). Mice were trained by a $\Delta 30^\circ$ task of 30% contrast gratings without noise. External visual noise (in 30%, 50%, or 70% contrast) was introduced into the gratings in the testing step (Figure 5R). The results showed that the *d'* of wild-type mice were significantly larger than that of *Opn4*^{-/-} mice when the stimuli were interfered by external noise. The absolute of *d'* slope to increasing noise was smaller for wild-type mice (0.8) than for *Opn4*^{-/-} mice (1.4) (Figure 5S), suggesting that wild-type mice maintain better orientation discrimination when stimuli are interfered by higher visual noise than *Opn4*^{-/-} mice.

Light activation of ipRGCs improves human visual orientation discrimination

We further investigated the contribution of ipRGCs to human visual orientation discrimination. To specifically manipulate the activity of ipRGCs in human, we used a light-spectrum-manipulating method (receptor silent substitution, see STAR Methods) to identify a specific spectral pair (“metameric” pair) that is indistinguishable from each type of cone but contains significant contrast for ipRGCs. The metameric pair includes a “reference” spectrum with lower and a “melanopic” spectrum with higher effective radiance to activate ipRGCs (see STAR Methods).^{50–52} For this purpose, we modified two projectors by inserting band-pass filters into their light paths to construct a four-primary-color display (violet, cyan, green, and red) that allowed the control the effective radiance to activate ipRGCs and each type of cone individually (Figures 6A and S6A). We then calculated the theoretical standard metameric pair by the published spectral sensitivity of

ipRGCs and three types of cones. The theoretical standard metameric pair consists of a reference spectrum with low effective radiance to activate ipRGCs (melanopic radiance = 0.11 W/m²/sr) and a melanopic spectrum with high effective radiance to activate ipRGCs (melanopic radiance = 0.16 W/m²/sr). Considering the inter-individual variations in cone spectral sensitivity and pre-receptor filtering, we therefore generated 169 variants of these pairs by making small alterations to the spectral composition of the melanopic spectrum while keeping the reference spectrum unchanged (Figure 6C; see STAR Methods), and then we tested those pairs on each participant to identify the specific customized metameric pair (Figures S6B–S6D; see STAR Methods). The radiance of each stimulus was at a photopic level under which rods were saturated.

Participants were seated in front of the projection screen in a dark room and asked to fixate their left eyes (right eyes were covered with eye patches) on a fixation dot on the screen (Figure 6B). Stimuli were all circular sinusoidal gratings (15° diameter) presented at 20° retinal eccentricity. For each participant, we proportionally mixed the reference and melanopic spectra in the customized metameric pair to generate three testing spectra that were indistinguishable by that individual participant to the image-forming photoreceptors (rods and cones) but activate ipRGCs differently (normalized ipRGC radiance: low = 1, mid = 1.1, high = 1.3) (Figure 6D). Under each testing spectra that differed in their activation of ipRGCs, participants were asked to identify the orientation difference of gratings (Figures 6B and S6E; see STAR Methods). Consistent with the results of animal experiments, the testing spectra with higher ipRGC activation significantly improved the orientation discriminability of human participants (Figure 6E), revealing that light activation of ipRGCs would also improve human visual sensitivity to small orientation differences.

Figure 5. Light activation of ipRGCs improves orientation discrimination in mice

- (A) Schematic of Go/No-Go behavioral experiment. Mouse licking when the Go stimulus is present will get a drop of water as reward (Hit), while licking when the No-Go stimulus is present will get air puff as punishment (false alarm, FA). Mice who take no action when either the Go (Miss) or No-Go (correct reject, CR) is present will get neither reward nor punishment.
- (B) Left: training protocol. Right: the performance (*d'*) of a representative mouse during the training step. The mouse reached steady performance after tens of training sessions.
- (C) Left: testing protocol. Right: the performances (*d'*) of a representative mouse in all tasks were fitted to obtain the orientation discrimination threshold where the fitted *d'* = 1.
- (D and E) *d'* of *Opn4*^{+/+} and *Opn4*^{-/-} mice at 6 different testing tasks. Data are mean \pm SEM. Rank-sum test.
- (F) Orientation discrimination threshold of *Opn4*^{+/+} and *Opn4*^{-/-} mice. Data are mean \pm SEM. Rank-sum test.
- (G) Schematic diagram of melanopsin or GFP expression in ipRGCs from *Opn4*^{-/-}; *Opn4*-Cre mice.
- (H) The *d'* of *Opn4*^{-/-}; *Opn4*-Cre mice at 6 different testing tasks before and after melanopsin or GFP expression in ipRGCs. Signed-rank test.
- (I) Orientation discrimination threshold of *Opn4*^{-/-}; *Opn4*-Cre mice before and after melanopsin or GFP expression in ipRGCs. Signed-rank test.
- (J) Schematic diagram of Go/No-Go testing of *Opn4*^{+/+} and *Opn4*^{-/-} mice to blue-rich or blue-less drifting gratings.
- (K) The *d'* of *Opn4*^{+/+} and *Opn4*^{-/-} mice to task $\Delta 10^\circ$ with blue-rich or blue-less stimulus. Signed-rank test.
- (L and M) The *d'* of *Opn4*^{-/-}; *Opn4*-Cre mice to blue-rich and blue-less stimuli at task $\Delta 10^\circ$ after melanopsin or GFP expression. Signed-rank test.
- (N) Schematic diagram of drifting gratings mixed with different contrast levels of black-and-white visual noise (0%, 30%, 50%, and 70%).
- (O) Schematic diagram of applying a linear decoder to neural population responses to measure the mouse discriminability. The purple vector represents the orientation of the external stimulus. The directions of blue vectors represented the decoded preferred orientations for the recorded neuronal population, and the magnitudes of blue vectors referred to the neuronal Ca²⁺ responses to drifting gratings in orientation of 90°. The direction of the sum of blue vectors is the decoded orientation of the recorded neuronal population (red vector). The angle of the yellow-filled part between the decoded (red vector) and external (purple vector) orientation represented the discrimination bias of decoded and visual orientations.
- (P) The decoded orientation biases to gratings interfered by different noise of *Opn4*^{+/+} and *Opn4*^{-/-} mice. Data are mean \pm SEM. Rank-sum test.
- (Q and R) Schematic diagram of Go/No-Go testing of *Opn4*^{+/+} and *Opn4*^{-/-} mice to gratings mixed with different levels of visual noise.
- (S) The *d'* of *Opn4*^{+/+} and *Opn4*^{-/-} mice to gratings interfered by different noise. The *d'* of *Opn4*^{+/+} mice were significantly larger than *Opn4*^{-/-} mice. The absolute of *d'* slope to increasing noise of *Opn4*^{+/+} mice (0.8) was smaller than that of *Opn4*^{-/-} mice (1.4). Data are mean \pm SEM. Rank-sum test.
- **p* < 0.05, ***p* < 0.01, ****p* < 0.001; n.s., no significant difference. See Table S2 for results of statistics.

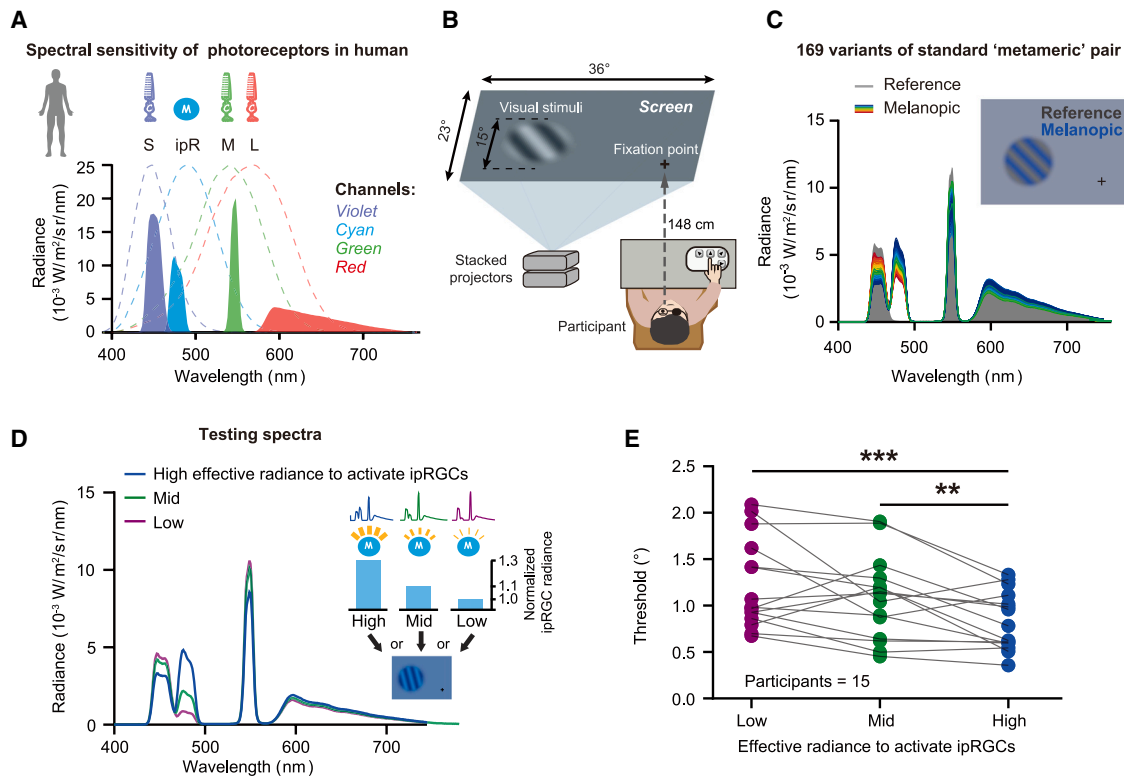


Figure 6. Light activation of ipRGCs improves human orientation discrimination

(A) Spectral power distributions of the four light channels (solid curves in violet, cyan, green, and red) and normalized spectral sensitivities of S, M, and L cones and ipRGCs in human retina (dashed lines in violet, green, red, and cyan). S, S cone; ipR, ipRGC; M, M cone; L, L cone.

(B) Schematic diagram of visual stimuli presentation in psychophysical experiment.

(C) Spectral power distributions of reference (gray) and melanopic spectra (colored lines, $n = 169$) used to identify a specific metameric pair for each participant individually. The variants of the standard metameric pair were generated by slightly alternating the melanopic spectrum, while the reference spectrum was consistent. For each pair, the grating stimulus was generated by mixing the reference and melanopic spectra alternately into a sinusoid pattern, while the background spectrum was the mean of reference and melanopic spectra.

(D) Spectral power distributions of 3 testing spectra with different effective radiance to activate ipRGCs but the same to each type of cone for a representative participant.

(E) Participants showed significantly lower thresholds of orientation discrimination for spectra with higher effective radiance to activate ipRGCs. Repeated one-way ANOVA followed by multiple comparisons.

* $p < 0.05$, ** $p < 0.01$, *** $p < 0.001$; n.s., no significant difference. See Table S2 for results of statistics.

DISCUSSION

Here, we revealed that ipRGCs differentially influence the response of V1 excitatory and inhibitory neurons, leading to a re-shaping of the cortical excitatory and inhibitory balance to improve visual feature processing, which consequently improves both mouse and human visual orientation discriminability.

Orientation selectivity is computed at multiple stages along the visual pathway. Although a subpopulation of the retina ganglion cells also shows orientation selectivity,⁵³ it is generally acknowledged that the neural processing steps generating orientation selectivity first take place in the dLGN⁵⁴ and then are well shaped in V1 L2/3 neurons through complex processing of the neuronal network.⁴⁷ Previous studies have shown that the intrinsic phototransduction of melanopsin amplifies contrast signals originating from rods and cones to ipRGCs in mouse retina,^{27–29} and ipRGCs send coarse RF information to

the mouse visual thalamus.^{52,55} The effects of ipRGCs to RF properties in retina and dLGN may contribute to the ipRGC-improved cortical orientation selectivity at the early image visual pathway.

The activation of V1 interneurons sharpens cortical neuronal feature selectivity and improves visual perceptual discrimination.^{46–48,56} Our results reveal that light activation of ipRGCs excites a large amount of interneurons at V1 and increases the response of interneurons to stimuli at all orientations, implying that ipRGCs may drive a broadly cortical inhibition to V1 to narrow tuning bandwidth as well as to improve orientation perception. In addition, our results further reveal that light activation of ipRGCs excites, on average, 75% of interneurons in V1 L1. Cortical L1 is thought to receive top-down information from other brain areas and dramatically modulates cortical feature processing depending on expectations^{57–59} or cross-modal interactions,^{60,61} and the excitatory inputs from ipRGCs to L1

interneurons suggests that light may influence cortical top-down information integration.

Previous studies on several subtypes of ipRGCs, namely M1–M6,^{62,63} have suggested that M4 and M5 constitute the majority of ipRGCs, which connect dLGN.^{64–66} M4 ipRGCs are subtypes of ON alpha ganglion cells, the conventional image-forming vision RGCs.^{27,29} Why some of the conventional RGCs express melanopsin and project to image-forming visual thalamus has long been puzzled. Our work demonstrates that melanopsin-dependent light input is necessary to improve cortical orientation selectivity, prompting us to consider ipRGCs as a new visual input component to better understand the image processing mechanism and highlighting the importance of spectrum design in both visual perception measurements and optimization of the environmental lighting.

RESOURCE AVAILABILITY

Lead contact

Requests for further information and for resources and reagents should be directed to and will be fulfilled by the lead contact, Tian Xue (xuetian@ustc.edu.cn).

Materials availability

This study did not generate new unique reagents.

Data and code availability

- Behavioral and two-photon Ca^{2+} imaging raw data have been deposited at Mendeley Data and are publicly available as of the date of publication. Accession numbers are listed in the [key resources table](#).
- This paper does not report original code.
- Any additional information required to reanalyze the data reported in this paper is available from the [lead contact](#) upon request.

ACKNOWLEDGMENTS

We thank Prof. Michael Stryker from University of California at San Francisco, Prof. Wei Wei from University of Chicago, Prof. Wei Li from National Institutes of Health, Prof. Xiaohui Zhang from Beijing Normal University, Prof. Yupeng Yang from University of Science and Technology of China, Prof. Xin Duan from University of California at San Francisco, Prof. Minmin Luo from National Institute of Biological Science, Prof. Yunyun Han from Huazhong University of Science and Technology, and Prof. Ye Li for critical comments on the manuscript, as well as Prof. Haohong Li from Huazhong University of Science and Technology for technical help in mouse behavior. We thank the following organizations for help funding this work: the National Key Research and Development Program of China (2020YFA0112200), Science and Technology Innovation 2030—Major Program (2022ZD0210000, 2021ZD0203100, 2021ZD0203700, and 2021ZD0203705), the Strategic Priority Research Program of the Chinese Academy of Science (XDB39050300), the CAS Project for Young Scientists in Basic Research (YSBR-013, YSBR-041, and YSBR-097), the Feng Foundation of Biomedical Research, the National Natural Science Foundation of China (32400848, 32471079, 323B1011, 32241010, 81925009, 32121002, 31925018, 32127801, 82201230, and T2122016), the Guangdong Basic and Applied Basic Research Foundation (2020B1515120014), the Tencent Foundation through the XPLOER PRIZE, and the New Cornerstone Science Foundation.

AUTHOR CONTRIBUTIONS

Conceptualization, T.X.; methodology, Y.S., J.Z., X. Li, Y.H., J.G., Y.L., J.S., T.T., D.Y., X. Luo, Y.Y., Z.C., T.W., Z.C., Y.M., Y.L., Q.W., J.H., J.M., X.L., Y.Z., L.T., Y. Ma, J.C., M.Z., R.L., Y. Miao, J.B., Z.L., X.C., and T.X.; investiga-

tion, Y.S., J.Z., R.L., Y. Mi, J.B., Z.L., X.C., and T.X.; visualization, Y.S., J.Z., R.L., Y. Mi, J.B., Z.L., X.C., and T.X.; funding acquisition, Y. Mi, X.C., and T.X.; project administration, T.X.; supervision, R.L., Y. Mi, J.B., Z.L., X.C., and T.X.; writing – original draft, Y.S., J.Z., R.L., Y. Mi, J.B., Z.L., X.C., and T.X.; writing – review & editing, Y.S., R.L., Y. Mi, J.B., Z.L., X.C., and T.X.

DECLARATION OF INTERESTS

The authors declare no competing interests.

STAR★METHODS

Detailed methods are provided in the online version of this paper and include the following:

- [KEY RESOURCES TABLE](#)
- [EXPERIMENTAL MODEL AND STUDY PARTICIPANT DETAILS](#)
 - Animals
 - Participants
- [METHOD DETAILS](#)
 - Viruses
 - Short hairpin RNA
 - Intravitreal injection
 - Stereotaxic injection
 - Histology
 - Quantitative real-time polymerase chain reaction
 - Two-photon Ca^{2+} imaging
 - Electrophysiology
 - Chemogenetic inhibition
 - Pupillary light reflex
 - Visual stimulation for mouse model
 - Two-photon data analysis
 - Multi-channel recording data analysis
 - The CANN models
 - Mouse behavioral experiment
 - Procedure for human visual orientation discrimination
- [QUANTIFICATION AND STATISTICAL ANALYSIS](#)

SUPPLEMENTAL INFORMATION

Supplemental information can be found online at <https://doi.org/10.1016/j.neuron.2024.11.015>.

Received: November 9, 2023

Revised: June 13, 2024

Accepted: November 22, 2024

Published: December 17, 2024

REFERENCES

1. Chang, L., and Tsao, D.Y. (2017). The Code for Facial Identity in the Primate Brain. *Cell* 169, 1013–1020.e14.
2. Simoncelli, E.P., and Olshausen, B.A. (2001). Natural image statistics and neural representation. *Annu. Rev. Neurosci.* 24, 1193–1216. <https://doi.org/10.1146/annurev.neuro.24.1.1193>.
3. Olshausen, B.A., and Field, D.J. (1996). Emergence of simple-cell receptive field properties by learning a sparse code for natural Images. *Nature* 381, 607–609. <https://doi.org/10.1038/381607a0>.
4. Do, M.T.H., and Yau, K.-W. (2010). Intrinsically photosensitive retinal ganglion cells. *Physiol. Rev.* 90, 1547–1581. <https://doi.org/10.1152/physrev.00013.2010>.
5. Lucas, R.J., Hattar, S., Takao, M., Berson, D.M., Foster, R.G., and Yau, K.W. (2003). Diminished pupillary light reflex at high irradiances in melanopsin-knockout mice. *Science* 299, 245–247. <https://doi.org/10.1126/science.1077293>.

6. Hattar, S., Lucas, R.J., Mrosovsky, N., Thompson, S., Douglas, R.H., Hankins, M.W., Lem, J., Biel, M., Hofmann, F., Foster, R.G., and Yau, K.W. (2003). Melanopsin and rod–cone photoreceptive systems account for all major accessory visual functions in mice. *Nature* 424, 76–81. <https://doi.org/10.1038/nature01761>.
7. Berson, D.M., Dunn, F.A., and Takao, M. (2002). Phototransduction by Retinal Ganglion Cells That Set the Circadian Clock. *Science* 295, 1070–1073. <https://doi.org/10.1126/science.1067262>.
8. Panda, S., Sato, T.K., Castrucci, A.M., Rollag, M.D., DeGrip, W.J., Hogenesch, J.B., Provencio, I., and Kay, S.A. (2002). Melanopsin (Opn4) requirement for normal light-induced circadian phase shifting. *Science* 298, 2213–2216. <https://doi.org/10.1126/science.1076848>.
9. An, K., Zhao, H., Miao, Y., Xu, Q., Li, Y.-F., Ma, Y.-Q., Shi, Y.-M., Shen, J.-W., Meng, J.-J., Yao, Y.-G., et al. (2020). A circadian rhythm-gated subcortical pathway for nighttime-light-induced depressive-like behaviors in mice. *Nat. Neurosci.* 23, 869–880. <https://doi.org/10.1038/s41593-020-0640-8>.
10. Huang, X., Tao, Q., and Ren, C. (2024). A Comprehensive Overview of the Neural Mechanisms of Light Therapy. *Neurosci. Bull.* 40, 350–362. <https://doi.org/10.1007/s12264-023-01089-8>.
11. Li, X., and Li, X. (2018). The Antidepressant Effect of Light Therapy from Retinal Projections. *Neurosci. Bull.* 34, 359–368. <https://doi.org/10.1007/s12264-018-0210-1>.
12. Fernandez, D.C., Fogerson, P.M., Lazzarini Ospri, L., Thomsen, M.B., Layne, R.M., Severin, D., Zhan, J., Singer, J.H., Kirkwood, A., Zhao, H., et al. (2018). Light Affects Mood and Learning through Distinct Retina-Brain Pathways. *Cell* 175, 71–84.e18. <https://doi.org/10.1016/j.cell.2018.08.004>.
13. Legates, T.A., Altimus, C.M., Wang, H., Lee, H.K., Yang, S., Zhao, H., Kirkwood, A., Weber, E.T., and Hattar, S. (2012). Aberrant light directly impairs mood and learning through melanopsin-expressing neurons. *Nature* 491, 594–598. <https://doi.org/10.1038/nature11673>.
14. Huang, L., Xi, Y., Peng, Y., Yang, Y., Huang, X., Fu, Y., Tao, Q., Xiao, J., Yuan, T., An, K., et al. (2019). A Visual Circuit Related to Habenula Underlies the Antidepressive Effects of Light Therapy. *Neuron* 102, 128–142.e8. <https://doi.org/10.1016/j.neuron.2019.01.037>.
15. Wang, G., Liu, Y.F., Yang, Z., Yu, C.X., Tong, Q., Tang, Y.L., Shao, Y.Q., Wang, L.Q., Xu, X., Cao, H., et al. (2023). Short-term acute bright light exposure induces a prolonged anxiogenic effect in mice via a retinal ipRGC-CeA circuit. *Sci. Adv.* 9, ead4651. <https://doi.org/10.1126/sciadv.adf4651>.
16. Renna, J.M., Weng, S., and Berson, D.M. (2011). Light acts through melanopsin to alter retinal waves and segregation of retinogeniculate afferents. *Nat. Neurosci.* 14, 827–829. <https://doi.org/10.1038/nn.2845>.
17. Kirkby, L.A., and Feller, M.B. (2013). Intrinsically photosensitive ganglion cells contribute to plasticity in retinal wave circuits. *Proc. Natl. Acad. Sci. USA* 110, 12090–12095. <https://doi.org/10.1073/pnas.1222150110>.
18. Rao, S., Chun, C., Fan, J., Kofron, J.M., Yang, M.B., Hegde, R.S., Ferrara, N., Copenhagen, D.R., and Lang, R.A. (2013). A direct and melanopsin-dependent fetal light response regulates mouse eye development. *Nature* 494, 243–246. <https://doi.org/10.1038/nature11823>.
19. Chew, K.S., Renna, J.M., McNeill, D.S., Fernandez, D.C., Keenan, W.T., Thomsen, M.B., Ecker, J.L., Loevinsohn, G.S., Vandunk, C., Vicarel, D.C., et al. (2017). A subset of ipRGCs regulates both maturation of the circadian clock and segregation of retinogeniculate projections in mice. *eLife* 6, e22861. <https://doi.org/10.7554/eLife.22861>.
20. Tufford, A.R., Onyak, J.R., Sondereker, K.B., Lucas, J.A., Earley, A.M., Mattar, P., Hattar, S., Schmidt, T.M., Renna, J.M., and Cayouette, M. (2018). Melanopsin Retinal Ganglion Cells Regulate Cone Photoreceptor Lamination in the Mouse Retina. *Cell Rep.* 23, 2416–2428. <https://doi.org/10.1016/j.celrep.2018.04.086>.
21. Liu, A.L., Liu, Y.F., Wang, G., Shao, Y.Q., Yu, C.X., Yang, Z., Zhou, Z.R., Han, X., Gong, X., Qian, K.W., et al. (2022). The role of ipRGCs in ocular growth and myopia development. *Sci. Adv.* 8, eabm9027. <https://doi.org/10.1126/sciadv.abm9027>.
22. Hu, J., Shi, Y., Zhang, J., Huang, X., Wang, Q., Zhao, H., Shen, J., Chen, Z., Song, W., Zheng, P., et al. (2022). Melanopsin retinal ganglion cells mediate light-promoted brain development. *Cell* 185, 3124–3137.e15. <https://doi.org/10.1016/j.cell.2022.07.009>.
23. Lazzarini Ospri, L., Zhan, J.J., Thomsen, M.B., Wang, H., Komal, R., Tang, Q., Messanvi, F., du Hoffmann, J., Cravedi, K., Chudasama, Y., et al. (2024). Light affects the prefrontal cortex via intrinsically photosensitive retinal ganglion cells. *Sci. Adv.* 10, eadh9251. <https://doi.org/10.1126/sciadv.adh9251>.
24. Rupp, A.C., Ren, M., Altimus, C.M., Fernandez, D.C., Richardson, M., Turek, F., Hattar, S., and Schmidt, T.M. (2019). Distinct ipRGC subpopulations mediate light's acute and circadian effects on body temperature and sleep. *eLife* 8, e44358. <https://doi.org/10.7554/eLife.44358>.
25. Meng, J.J., Shen, J.W., Li, G., Ouyang, C.J., Hu, J.X., Li, Z.S., Zhao, H., Shi, Y.M., Zhang, M., Liu, R., et al. (2023). Light modulates glucose metabolism by a retina-hypothalamus-brown adipose tissue axis. *Cell* 186, 398–412.e17. <https://doi.org/10.1016/j.cell.2022.12.024>.
26. Rao, F., and Xue, T. (2024). Circadian-independent light regulation of mammalian metabolism. *Nat. Metab.* 6, 1000–1007. <https://doi.org/10.1038/s42255-024-01051-6>.
27. Sonoda, T., Lee, S.K., Birnbaumer, L., Schmidt, T.M., Sonoda, T., Lee, S.K., Birnbaumer, L., and Schmidt, T.M. (2018). Melanopsin Phototransduction Is Repurposed by ipRGC Subtypes to Shape the Function of Distinct Visual. *Neuron* 99, 754–767.e4.
28. Ecker, J.L., Dumitrescu, O.N., Wong, K.Y., Alam, N.M., Chen, S.K., Legates, T., Renna, J.M., Prusky, G.T., Berson, D.M., and Hattar, S. (2010). Melanopsin-Expressing Retinal Ganglion-Cell Photoreceptors: Cellular Diversity and Role in Pattern Vision. *Neuron* 67, 49–60. <https://doi.org/10.1016/j.neuron.2010.05.023>.
29. Schmidt, T.M., Alam, N.M., Chen, S., Kofuji, P., Li, W., Prusky, G.T., and Hattar, S. (2014). A Role for Melanopsin in Alpha Retinal Ganglion Cells and Contrast Detection. *Neuron* 82, 781–788. <https://doi.org/10.1016/j.neuron.2014.03.022>.
30. Dacey, D.M., Liao, H.W., Peterson, B.B., Robinson, F.R., Smith, V.C., Pokorny, J., Yau, K.W., and Gamlin, P.D. (2005). Melanopsin-expressing ganglion cells in primate retina signal colour and irradiance and project to the LGN. *Nature* 433, 749–754. <https://doi.org/10.1038/nature03387>.
31. Storchi, R., Milosavljevic, N., Eleftheriou, C.G., Martial, F.P., Orłowska-Feuer, P., Bedford, R.A., Brown, T.M., Montemurro, M.A., Petersen, R.S., and Lucas, R.J. (2015). Melanopsin-driven increases in maintained activity enhance thalamic visual response reliability across a simulated dawn. *Proc. Natl. Acad. Sci. USA* 112, E5734–E5743. <https://doi.org/10.1073/pnas.1505274112>.
32. Allen, A.E., Storchi, R., Martial, F.P., Bedford, R.A., and Lucas, R.J. (2017). Melanopsin Contributions to the Representation of Images in the Early Visual System. *Curr. Biol.* 27, 1623–1632.e4. <https://doi.org/10.1016/j.cub.2017.04.046>.
33. Storchi, R., Bedford, R.A., Martial, F.P., Allen, A.E., Wynne, J., Montemurro, M.A., Petersen, R.S., Lucas, R.J., Storchi, R., and Bedford, R.A. (2017). Modulation of Fast Narrowband Oscillations in the Mouse Retina and dLGN According to Background Light Intensity. *Neuron* 93, 299–307. <https://doi.org/10.1016/j.neuron.2016.12.027>.
34. Davis, K.E., Eleftheriou, C.G., Allen, A.E., Procyk, C.A., and Lucas, R.J. (2015). Melanopsin-Derived Visual Responses under Light Adapted Conditions in the Mouse dLGN. *PLoS One* 10, e0123424. <https://doi.org/10.1371/journal.pone.0123424>.
35. Allen, A.E., Storchi, R., Martial, F.P., Petersen, R.S., Montemurro, M.A., Brown, T.M., and Lucas, R.J. (2014). Melanopsin-Driven Light Adaptation in Mouse Vision. *Curr. Biol.* 24, 2481–2490. <https://doi.org/10.1016/j.cub.2014.09.015>.

36. Stosiek, C., Garaschuk, O., Holthoff, K., and Konnerth, A. (2003). In vivo two-photon calcium imaging of neuronal networks. *Proc. Natl. Acad. Sci. USA* *100*, 7319–7324. <https://doi.org/10.1073/pnas.1232232100>.
37. Li, J., Zhang, J., Wang, M., Pan, J., Chen, X., and Liao, X. (2017). Functional imaging of neuronal activity of auditory cortex by using Cal-520 in anesthetized and awake mice. *Biomed. Opt. Express* *8*, 2599–2610. <https://doi.org/10.1364/BOE.8.002599>.
38. Hubel, D.H., and Wiesel, T.N. (1962). Receptive fields, binocular interaction and functional architecture in the cat's visual cortex. *J. Physiol.* *160*, 106–154. <https://doi.org/10.1113/jphysiol.1962.sp006837>.
39. Tring, E., Duan, K.K., and Ringach, D.L. (2022). ON/OFF domains shape receptive field structure in mouse visual cortex. *Nat. Commun.* *13*, 2466. <https://doi.org/10.1038/s41467-022-29999-7>.
40. Kremkow, J., Jin, J., Wang, Y., and Alonso, J.M. (2016). Principles underlying sensory map topography in primate visual cortex. *Nature* *533*, 52–57. <https://doi.org/10.1038/nature17936>.
41. Zhao, X., Chen, H., Liu, X., and Cang, J. (2013). Orientation-selective responses in the mouse lateral geniculate nucleus. *J. Neurosci.* *33*, 12751–12763. <https://doi.org/10.1523/JNEUROSCI.0095-13.2013>.
42. Priebe, N.J. (2016). Mechanisms of Orientation Selectivity in the Primary Visual Cortex. *Annu. Rev. Vis. Sci.* *2*, 85–107. <https://doi.org/10.1146/annurev-vision-111815-114456>.
43. Li, Y.T., Liu, B.H., Chou, X.L., Zhang, L.I., and Tao, H.W. (2015). Synaptic basis for differential orientation selectivity between complex and simple cells in mouse visual cortex. *J. Neurosci.* *35*, 11081–11093. <https://doi.org/10.1523/JNEUROSCI.5246-14.2015>.
44. Liao, H.W., and Yau, K.W. (2007). In vivo gene delivery in the retina using polyethylenimine. *BioTechniques* *42*, 285–288. <https://doi.org/10.2144/000112404>.
45. Priebe, N.J., and Ferster, D. (2008). Inhibition, Spike Threshold, and Stimulus Selectivity in Primary Visual Cortex. *Neuron* *57*, 482–497. <https://doi.org/10.1016/j.neuron.2008.02.005>.
46. Liu, B.H., Li, Y.T., Ma, W.P., Pan, C.J., Zhang, L.I., and Tao, H.W. (2011). Broad Inhibition Sharpens Orientation Selectivity By Expanding Input Dynamic Range in Mouse Simple Cells. *Neuron* *71*, 542–554. <https://doi.org/10.1016/j.neuron.2011.06.017>.
47. Isaacson, J.S., and Scanziani, M. (2011). How Inhibition Shapes Cortical Activity. *Neuron* *72*, 231–243. <https://doi.org/10.1016/j.neuron.2011.09.027>.
48. Lee, S.H., Kwan, A.C., Zhang, S., Phoumthipphavong, V., Flannery, J.G., Masmanidis, S.C., Taniguchi, H., Huang, Z.J., Zhang, F., Boyden, E.S., et al. (2012). Activation of specific interneurons improves V1 feature selectivity and visual perception. *Nature* *488*, 379–383. <https://doi.org/10.1038/nature11312>.
49. Ben-Yishai, R., Bar-Or, R.L., and Sompolinsky, H. (1995). Theory of orientation tuning in visual cortex. *Proc. Natl. Acad. Sci. USA* *92*, 3844–3848. <https://doi.org/10.1073/pnas.92.9.3844>.
50. Allen, A.E., Hazelhoff, E.M., Martial, F.P., Cajochen, C., and Lucas, R.J. (2018). Exploiting metamerism to regulate the impact of a visual display on alertness and melatonin suppression independent of visual appearance. *Sleep* *41*, 1–7. <https://doi.org/10.1093/sleep/zsy100>.
51. Spitschan, M., Bock, A.S., Ryan, J., Frazzetta, G., Brainard, D.H., and Aguirre, G.K. (2017). The human visual cortex response to melanopsin-directed stimulation is accompanied by a distinct perceptual experience. *Proc. Natl. Acad. Sci. USA* *114*, 12291–12296. <https://doi.org/10.1073/pnas.1711522114>.
52. Allen, A.E., Martial, F.P., and Lucas, R.J. (2019). Form vision from melanopsin in humans. *Nat. Commun.* *10*, 2274. <https://doi.org/10.1038/s41467-019-10113-3>.
53. Antinucci, P., Suleyman, O., Monfries, C., and Hindges, R. (2016). Neural Mechanisms Generating Orientation Selectivity in the Retina. *Curr. Biol.* *26*, 1802–1815. <https://doi.org/10.1016/j.cub.2016.05.035>.
54. Scholl, B., Tan, A.Y.Y., Corey, J., and Priebe, N.J. (2013). Emergence of Orientation Selectivity in the Mammalian Visual Pathway. *J. Neurosci.* *33*, 10616–10624. <https://doi.org/10.1523/JNEUROSCI.0404-13.2013>.
55. Moulard, J.W., Stinchcombe, A.R., Forger, D.B., Brown, T.M., and Lucas, R.J. (2017). Responses to Spatial Contrast in the Mouse Suprachiasmatic Nuclei. *Curr. Biol.* *27*, 1633–1640.e3. <https://doi.org/10.1016/j.cub.2017.04.039>.
56. Alitto, H.J., and Dan, Y. (2010). Function of Inhibition in Visual Cortical Processing. *Curr. Opin. Neurobiol.* *20*, 340–346. <https://doi.org/10.1016/j.conb.2010.02.012>.
57. Schroeder, A., Bele, M., Keijser, J., Schuman, E.M., Sprekeler, H., and Letzkus, J.J. (2023). Inhibitory top-down projections from zona incerta mediate neocortical memory. *Neuron* *111*, 1–2.
58. Malina, K.C., Tsivourakis, E., Kushinsky, D., Mizrahi, A., Malina, K.C., Tsivourakis, E., Kushinsky, D., Apelblat, D., and Shtiglit, S. (2021). NDNF interneurons in layer 1 gain-modulate whole cortical columns according to an animal's behavioral state. *Neuron* *109*, 2150–2164.e5.
59. Hu, F., Kamigaki, T., Zhang, Z., Zhang, S., Dan, U., Dan, Y., Hu, F., Kamigaki, T., Zhang, Z., Zhang, S., et al. (2019). Prefrontal Corticotectal Neurons Enhance Visual Processing through the Superior Colliculus and Pulvinar Thalamus Article Prefrontal Corticotectal Neurons Enhance Visual Processing through the Superior Colliculus and Pulvinar Thalamus. *Neuron* *104*, 1141–1152.e4.
60. Ibrahim, L.A., Mesik, L., Ji, X.Y., Fang, Q., Li, H.F., Li, Y.T., Zingg, B., Zhang, L.I., and Tao, H.W. (2016). Cross-Modality Sharpening of Visual Cortical Processing through Layer-1-Mediated Inhibition and Disinhibition. *Neuron* *89*, 1031–1045. <https://doi.org/10.1016/j.neuron.2016.01.027>.
61. Chou, X.L., Fang, Q., Yan, L., Zhong, W., Peng, B., Li, H., Wei, J., Tao, H.W., and Zhang, L.I. (2020). Contextual and cross-modality modulation of auditory cortical processing through pulvinar mediated suppression. *eLife* *9*, e54157. <https://doi.org/10.7554/eLife.54157>.
62. Schmidt, T.M., Chen, S.K., and Hattar, S. (2011). Intrinsically photosensitive retinal ganglion cells: many subtypes, diverse functions. *Trends Neurosci.* *34*, 572–580. <https://doi.org/10.1016/j.tins.2011.07.001>.
63. Quattrochi, L.E., Stabio, M.E., Kim, I., Ilardi, M.C., Michelle Fogerson, P., Leyrer, M.L., and Berson, D.M. (2019). The M6 cell: A small-field bistratified photosensitive retinal ganglion cell. *J. Comp. Neurol.* *527*, 297–311. <https://doi.org/10.1002/cne.24556>.
64. Aranda, M.L., and Schmidt, T.M. (2021). Diversity of intrinsically photosensitive retinal ganglion cells: circuits and functions. *Cell. Mol. Life Sci.* *78*, 889–907. <https://doi.org/10.1007/s00018-020-03641-5>.
65. Estevez, M.E., Fogerson, P.M., Ilardi, M.C., Borghuis, B.G., Chan, E., Weng, S., Auferkorte, O.N., Demb, J.B., and Berson, D.M. (2012). Form and function of the M4 cell, an intrinsically photosensitive retinal ganglion cell type contributing to geniculocortical vision. *J. Neurosci.* *32*, 13608–13620. <https://doi.org/10.1523/JNEUROSCI.1422-12.2012>.
66. Hattar, S., Kumar, M., Park, A., Tong, P., Tung, J., Yau, K.W., and Berson, D.M. (2006). Central Projections of Melanopsin- Expressing Retinal Ganglion Cells in the Mouse. *J. Comp. Neurol.* *497*, 326–349. <https://doi.org/10.1002/cne.20970>.
67. Hattar, S., Liao, H.W., Takao, M., Berson, D.M., and Yau, K.W. (2002). Melanopsin-Containing Retinal Ganglion Cells: Architecture, Projections, and Intrinsic Photosensitivity. *Science* *295*, 1065–1070. <https://doi.org/10.1126/science.1069609>.
68. Wang, Q., Yue, W.W.S., Jiang, Z., Xue, T., Kang, S.H., Bergles, D.E., Mikoshiba, K., Offermanns, S., and Yau, K.W. (2017). Synergistic Signaling by Light and Acetylcholine in Mouse Iris Sphincter Muscle. *Curr. Biol.* *27*, 1791–1800.e5. <https://doi.org/10.1016/j.cub.2017.05.022>.
69. Chen, X., Leischner, U., Varga, Z., Jia, H., Deca, D., Rochefort, N.L., and Konnerth, A. (2012). LOTOS-based two-photon calcium imaging of dendritic spines in vivo. *Nat. Protoc.* *7*, 1818–1829. <https://doi.org/10.1038/nprot.2012.106>.

70. Tada, M., Takeuchi, A., Hashizume, M., Kitamura, K., and Kano, M. (2014). A highly sensitive fluorescent indicator dye for calcium imaging of neural activity in vitro and in vivo. *Eur. J. Neurosci.* *39*, 1720–1728. <https://doi.org/10.1111/ejn.12476>.
71. Jia, H., Varga, Z., Sakmann, B., and Konnerth, A. (2014). Linear integration of spine Ca²⁺ signals in layer 4 cortical neurons in vivo. *Proc. Natl. Acad. Sci. USA* *111*, 9277–9282. <https://doi.org/10.1073/pnas.1408525111>.
72. Li, Z., Peng, B., Huang, J.J., Zhang, Y., Seo, M.B., Fang, Q., Zhang, G.W., Zhang, X., Zhang, L.I., and Tao, H.W. (2023). Enhancement and contextual modulation of visuospatial processing by thalamocollicular projections from ventral lateral geniculate nucleus. *Nat. Commun.* *14*, 7278. <https://doi.org/10.1038/s41467-023-43147-9>.
73. Niell, C.M., and Stryker, M.P. (2008). Highly Selective Receptive Fields in Mouse Visual Cortex. *J. Neurosci.* *28*, 7520–7536. <https://doi.org/10.1523/JNEUROSCI.0623-08.2008>.
74. Fang, Q., Chou, X., Peng, B., Zhong, W., Zhang, L.I., Fang, Q., Chou, X., Peng, B., Zhong, W., Zhang, L.I., et al. (2020). A Differential Circuit via Retino-Colliculo-Pulvinar Pathway Enhances Feature Selectivity in Visual Cortex through Surround Suppression. *Neuron* *105*, 355–369.e6.
75. Gao, E., DeAngelis, G.C., and Burkhalter, A. (2010). Parallel input channels to mouse primary visual cortex. *J. Neurosci.* *30*, 5912–5926. <https://doi.org/10.1523/JNEUROSCI.6456-09.2010>.
76. Rochefort, N.L., Narushima, M., Grienberger, C., Marandi, N., Hill, D.N., and Konnerth, A. (2011). Development of Direction Selectivity in Mouse Cortical Neurons. *Neuron* *71*, 425–432. <https://doi.org/10.1016/j.neuron.2011.06.013>.
77. Ringach, D.L., Shapley, R.M., and Hawken, M.J. (2002). Orientation Selectivity in Macaque V1: Diversity and Laminar Dependence. *J. Neurosci.* *22*, 5639–5651. <https://doi.org/10.1523/JNEUROSCI.22-13-05639.2002>.
78. Kerlin, A.M., Andermann, M.L., Berezovskii, V.K., and Reid, R.C. (2010). Broadly Tuned Response Properties of Diverse Inhibitory Neuron Subtypes in Mouse Visual Cortex. *Neuron* *67*, 858–871. <https://doi.org/10.1016/j.neuron.2010.08.002>.
79. Wu, S., Hamaguchi, K., and Amari, S.I. (2008). Dynamics and computation of continuous attractors. *Neural Comput.* *20*, 994–1025. <https://doi.org/10.1162/neco.2008.10-06-378>.
80. Wu, S., and Amari, S.I. (2005). Computing with continuous attractors: Stability and online aspects. *Neural Comput.* *17*, 2215–2239. <https://doi.org/10.1162/0899766054615626>.
81. Chen, X., and Li, H. (2017). ArControl: An Arduino-Based Comprehensive Behavioral Platform with Real-Time Performance. *Front. Behav. Neurosci.* *11*, 244. <https://doi.org/10.3389/fnbeh.2017.00244>.
82. Andermann, M.L., Kerlin, A.M., and Reid, R.C. (2010). Chronic cellular imaging of mouse visual cortex during operant behavior and passive viewing. *Front. Cell. Neurosci.* *4*, 3. <https://doi.org/10.3389/fncel.2010.00003>.
83. Solomon, S.G., and Lennie, P. (2007). The machinery of colour vision. *Nat. Rev. Neurosci.* *8*, 276–286. <https://doi.org/10.1038/nrn2094>.
84. Spitschan, M., and Woelders, T. (2018). The method of silent substitution for examining melanopsin contributions to pupil control. *Front. Neurol.* *9*, 941. <https://doi.org/10.3389/fneur.2018.00941>.
85. Spitschan, M., Aguirre, G.K., and Brainard, D.H. (2015). Selective stimulation of penumbral cones reveals perception in the shadow of retinal blood vessels. *PLoS One* *10*, e0124328. <https://doi.org/10.1371/journal.pone.0124328>.
86. CIE (2006). *Fundamental Chromaticity Diagram with Physiological Axes – Part 1 (CIE)*.
87. Govardovskii, V.I., Fyhrquist, N., Reuter, T., Kuzmin, D.G., and Donner, K. (2000). In search of the visual pigment template. *Vis. Neurosci.* *17*, 509–528. <https://doi.org/10.1017/s0952523800174036>.
88. Wetherill, G.B., and Levitt, H. (1965). Sequential estimation of points on a psychometric function. *Br. J. Math. Stat. Psychol.* *18*, 1–10. <https://doi.org/10.1111/j.2044-8317.1965.tb00689.x>.

STAR★METHODS

KEY RESOURCES TABLE

REAGENT or RESOURCE	SOURCE	IDENTIFIER
Antibodies		
Rabbit anti-melanopsin	Advanced Targeting System	Cat# AB-N38; RRID: AB_1266797
Rabbit anti-GABA	Sigma-Aldrich	Cat# A2052; RRID: AB_477652
Rabbit anti- Glutamate	Sigma-Aldrich	Cat# G6642; RRID: AB_259946
Alexa Fluor™ 568 goat anti-rabbit IgG	Thermo Fisher	Cat# A11036; RRID: AB_10563566
Bacterial and virus strains		
AAV2/2-hSyn-DIO-m <i>Opn4</i> -P2A-EGFP-WPRE-pA	Shanghai Taitool Bioscience Co.Ltd.	Cat# AAV2/2-XT327
AAV2/2-hSyn-DIO-hM4D(Gi)-mCherry-WPRE-pA	Shanghai Taitool Bioscience Co.Ltd.	Cat# S0193-2
AAV2/2-H1- <i>Opn4</i> shRNA-hSyn-EGFP-WPRE-pA	Shanghai Taitool Bioscience Co.Ltd.	N.A.
AAV2/2-H1-ffLuciferase shRNA-hSyn-EGFP-WPRE-pA	Shanghai Taitool Bioscience Co.Ltd.	Cat# S0970-2
AAV2/2-EF1 α -DIO-GFP-WPRE-pA	Vigene Biosciences, Inc	Cat# AV200096-AV2
AAV2/9-mDlx5/6-GCaMP6s-WPRE-pA	BrainVTA (Wuhan, China)	Cat# PT-2757
AAV2/9-CaMKII α -GCaMP6s-WPRE-pA	BrainVTA (Wuhan, China)	Cat# PT-0110
Chemicals, peptides, and recombinant proteins		
Atropine	Aladdin	Cat# A109524
(R)-(-)-Phenylephrine Hydrochloride	Aladdin	Cat# G1316011
Clozapine N-oxide	Sigma-Aldrich	Cat# 34233-69-7
Vitamins	Sigma-Aldrich	Cat# M6895
Non-essential Amino Acid Solution	Sigma-Aldrich	Cat# M7145
Isoflurane	Shenzhen RWD Life Science, China	Cat# R510-22-10
Tetrodotoxin	Dalian Refine Biochemical Items Company	N/A
Amphotericin B	MCE	Cat# HY-B0221
Triton X-100	Sangon Biotech	Cat# A110694-0100
Bovine albumin	Sangon Biotech	Cat# A600332-0100
2 × Taq Master Mix (Dye Plus)	Vazyme	Cat# P112-03
Optimal Cutting temperature (O.C.T) Compound	Sakura	Cat# 4583
Deposited data		
Behavioral, electrophysiological and morphological raw data	Mendeley Data	https://doi.org/10.17632/w2m36k4gkc.1
Experimental models: Organisms/strains		
Mouse: <i>rd1;cDTA</i>	Gift from King-Wai Yau in Johns Hopkins University	N/A
Mouse: <i>rd1;cDTA;Opn4^{-/-}</i>	Gift from King-Wai Yau in Johns Hopkins University	N/A
Mouse: <i>Opn4^{-/-}</i>	Hattar et al. ⁶⁷	N/A
Mouse: <i>Opn4-Cre</i>	Wang et al. ⁶⁸	N/A
Recombinant DNA		
The cDNA sequence for shRNA used for knocking down <i>Opn4</i> mRNA expression: 5'-ACGGTCATCTACACCTTCT-3'	Liao and Yau ⁴⁴	N/A
The primer for <i>Opn4</i> in real-time PCR: 5'-TCTACCCACCGCTCCACATT-3' (forward) and 5'-CCTGGCTCCCTGTCTTTCA-3' (reverse)	This paper	N/A

(Continued on next page)

Continued

REAGENT or RESOURCE	SOURCE	IDENTIFIER
The primer for <i>Gapdh</i> in real-time PCR: 5'-AGGTCGGTG TGAACGGATTTG-3' (forward) and 5'-TGTAGACCATGTAGTTGAGGTCA-3' (reverse)	This paper	N/A
Software and algorithms		
ImageJ	National Institutes of Health (NIH), USA	https://imagej.nih.gov/ij/download.html
MATLAB	MathWorks	https://www.mathworks.com/products/matlab.html
LAS X	Leica	https://www.leica-microsystems.com/products/microscope-software/details/product/leica-las-x-ls/
LabVIEW	National Instrument	http://www.ni.com/en-us/shop/labview/select-edition.html ; RRID: SCR_014325
OmniPlex Server	Plexon	https://plexon.com/plexon-systems/omniplex-neural-recording-system/#
PlexControl	Plexon	https://plexon.com/plexon-systems/omniplex-neural-recording-system/#
Offline Sorter	Plexon	https://plexon.com/products/offline-sorter/ Version 4.5.0
Other		
Nanofil syringe	World Precision Instrument	07K with 36G Blunt Needle
Dental acrylic	Super-Bond, C&B	https://sunmedical.co.jp/english/product/super-bond/cb-kit/index.html
MultiClamp 700B amplifier	Molecular Devices	https://www.moleculardevices.com/products/axon-patch-clamp-system/amplifiers/axon-instruments-patch-clamp-amplifiers
Leica SP8 scanning microscope	Leica, Germany	https://www.leica-microsystems.com.cn/cn/products/confocal-microscopes/p/leica-tcs-sp8/
Vibrating microtome	Leica, Germany	https://www.leicabiosystems.com/zh-cn/research/vibratomes/leica-vt1200/
Model 2100 Isolated Pulse Stimulator	AM-SYSTEM INC	MODEL 2100
LOTOS two-photon microscopy	Chen et al. ⁶⁹	LotosScan 1.0
LightCycler® 96 Instrument	Roche	Cat# 05815916001
64-channel electrode	NeuroNexus	A1x64-Poly2-6mm-23s-160-A64
OmniPlex Neural Recording Data Acquisition System	Plexon	https://plexon.com/plexon-systems/omniplex-neural-recording-system/#

EXPERIMENTAL MODEL AND STUDY PARTICIPANT DETAILS

Animals

All animal procedures were approved by the Institutional Animal Care and Use Committees at the University of Science and Technology of China (USTC) and the Chinese Academy of Sciences (CAS). Both female and male mice were used in each experiment. All C57BL/6J mice used in this study were obtained from SPF (Beijing) Biotechnology Co., Ltd. *Opn4^{-/-}*, *Opn4-Cre*, *rd1;cDTA* and *rd1;cDTA;Opn4^{-/-}* mice were general gifts from King-Wai Yau at Johns Hopkins University. The *rd1* (retinal degeneration 1) is a common retinal degeneration in mice, and mice homozygous for the *rd1* mutation have an early onset severe degeneration of rods. The *cDTA* mice endogenously express diphtheria toxin A (DTA) in cones. The rods and cones in *rd1;cDTA* mouse retina completely degenerate 2 months after birth. The *Opn4-Cre* mouse line in our manuscript is a gift from King-Wai Yau in Johns Hopkins University and has been published.⁶⁸ As described in Wang et al.,⁶⁸ for the generation of *Opn4-Cre* mouse line, the Cre recombinase cDNA, followed by the rabbit b-globin poly-A signal, were inserted immediately after the start codon in exon 1 of the mouse melanopsin

gene in a bacterial artificial chromosome (BAC) clone (BACPAC Resource Center, RP23-340N18) by bacterial homologous recombination. The modified BAC was linearized by enzyme digestion with *AscI* and *SrfI*, and subsequently injected into the pronuclei of B6SJLF2 embryos. Transgenic founders were identified by PCR on genomic DNA and were bred with wild-type C57BL/6J mice to establish transgenic lines. The *Opn4*^{-/-} mouse line was generated by replacing melanopsin gene (from exons 1 to 9) with tau-lacZ construct,⁶⁷ resulting in systematic knockout of melanopsin gene. The *rd1;cDTA;Opn4*^{-/-};*Opn4*-Cre and *Opn4*-Cre;*Opn4*^{-/-} mice were bred by animals above. The *rd1;cDTA*, *rd1;cDTA;Opn4*^{-/-} and *Opn4*-Cre;*rd1;cDTA;Opn4*^{-/-} mice used in this study were 3-5 months old to ensure the rods and cones completely degenerate. The *Opn4*^{-/-}, *Opn4*-Cre and *Opn4*^{-/-};*Opn4*-Cre mice used in this study are 2-4 months old.

Participants

The study was conducted according to the ethical guidelines of the First Affiliated Hospital of the University of Science and Technology of China and all the subjects signed informed consent to participate in the study (KY2021-091). Fifteen participants (eleven Chinese males, four Chinese females, mean age \pm SD = 26 \pm 3.7 years) were recruited from the University of Science and Technology of China. All participants had 20/20 or better visual acuity after correction and normal red-green color vision as assessed by the Ishihara test for the tested eye, and all of them had no known cognitive or neurological impairments. The experimental protocols followed the tenets of the Declaration of Helsinki and were approved by the Internal Review Board of the University of Science and Technology of China. Written informed consents were obtained from all participants prior to the experiment. Except one of the authors, all of the participants were naïve to the purposes of the tests.

METHOD DETAILS

No statistical methods were used to predetermine sample size. The experiments were randomized. The investigators were blinded to allocation during experiments and outcome assessment.

Viruses

The following fluorescent viral tools were employed in the current study: AAV2/2-hSyn-DIO-m*Opn4*-EGFP-WPRE-pA was used to Cre-dependently express melanopsin in ipRGCs of *Opn4*^{-/-};*Opn4*-Cre mice. AAV2/2-hSyn-DIO-hM4Di-mCherry-WPRE-pA was used to Cre-dependently express the inhibitory DREADDs hM4Di in ipRGCs of *Opn4*-Cre mice. AAV2/2-H1-*Opn4* shRNA-hSyn-EGFP-WPRE-pA was used to knock down the *Opn4* mRNA expression in the retina, and AAV2/2-H1-ffLuciferase shRNA-hSyn-EGFP-WPRE-pA was used as control. AAV2/2-EF1 α -DIO-GFP-WPRE-pA was used to Cre-dependently express GFP in ipRGCs for all control experiments. AAV2/9-mDlx5/6-GCaMP6s-WPRE-pA and AAV2/9-CaMKII α -GCaMP6s-WPRE-pA were used to express GCaMP6s in V1 inhibitory interneurons or excitatory pyramidal neurons respectively. AAV2/2-EF1 α -DIO-GFP-WPRE-pA was obtained from Vigene Biosciences, Inc. AAV2/9-mDlx5/6-GCaMP6s-WPRE-pA and AAV2/9-CaMKII α -GCaMP6s-WPRE-pA were obtained from BrainVTA (Wuhan, China). The other types of AAV were obtained from Shanghai Taitool Bioscience.

Short hairpin RNA

The cDNA sequence for shRNA used for knocking down melanopsin mRNA expression was: 5'-ACGGTCATCTACACCTTCT-3'.⁴⁴

Intravitreal injection

The dilating eye drop (1% w/v Atropin and 5% w/v Phenylephrine hydrochloride) was applied to dilate the pupils. After the pupils were fully dilated, mice were anesthetized with 1.5-2.0% isoflurane (Shenzhen RWD Life Science, China), afterwards eye gel (5% sodium carboxymethyl cellulose) was applied to prevent eyes from drying. The eyeball was then penetrated through the edge of cornea with the tip of a 26G needle under the stereoscope to release the ocular pressure, immediately followed by the injection of 1.5 μ l virus into the space between the lens and the retina using a Hamilton syringe (Model 65 RN SYR with 33G customized 48 needle). To minimize the damage to imaging vision, the tip of needle or Hamilton syringe was operated carefully without touching the retina and lens, and the ones with noticeable bleeding or damage to the retina or cornea were excluded from further experiments. Following surgery, mice were allowed to recover from anesthesia on a heating mat before being returned to their home cages.

Stereotaxic injection

Adult mouse was anesthetized with 1.5-2.0% isoflurane and mounted on a stereotaxic apparatus (Shenzhen RWD Life Science, China). Erythromycin ointment (Guangdong Hengjian Pharmaceutical Co.,Ltd, China) was applied to protect the eyes. The scalp was shaved and cleansed, then a linear incision on the skin was made to expose the skull which was subsequently cleaned with a cotton swab dipped in phosphate buffered saline (PBS). The skull above the target area was drilled open and virus was delivered into the brain at the rate of 30 nL/min as the following stereotaxic coordinates: V1 (AP: -3.5 mm from bregma; ML: -2.5 mm; DV: -0.5 mm). After completion of the injection including a 10 min delay, the injection pipette was slowly withdrawn and the scalp was sutured back.

Histology

Mice anesthetized with 1.5–2.0% isoflurane were perfused intracardially with PBS, followed by 4% paraformaldehyde (PFA, wt/vol in PBS). Then brain was removed, post-fixed in 4% PFA at 4°C for 24 h, and then dehydrated in 30% sucrose solution. Coronal sections were made on a Cryostat microtome (Leica CM3050S) at 50 μm thickness, blocked with blocking solution (PBS containing 5% BSA, 5% goat serum and 0.5% Triton X-100 as appropriate) for 1 h at room temperature and then incubated with the appropriate primary antibody (antibodies) for 24 h at 4°C. After the incubation with primary antibody, sections were washed with PBS (3 \times 5 min), then incubated with secondary antibodies for 1 h at room temperature. The brain slice was imaged under a Leica two-photon microscope (SP8, Leica, Germany).

For retinal immunostaining, the mice were euthanized by high concentration of carbon dioxide and then eyes were removed and fixed in 4% (wt/vol) paraformaldehyde for 2 h at room temperature. After the fixation, the cornea was cut off and the vitreous was cleaned up. Retina was then isolated and blocked with blocking solution (PBS containing 5% BSA, 5% Goat serum, and 0.5% Triton X-100 as appropriate) for 1 h at room temperature, then incubated with the appropriate primary antibody (antibodies) for 24 h at 4°C. Finally, the flat-mount retina was examined and imaged under a Leica two-photon microscope (SP8, Leica, Germany).

The primary antibodies used in the present study are as follows: Rabbit anti-melanopsin (Advanced Targeting System, Cat# AB-N38, 1: 1000; RRID: AB_1266797; Lot # 112-16); rabbit anti-GABA (Sigma-Aldrich Cat# A2052; 1:500; RRID: AB_477652; lot no. 018M4808V); rabbit anti-Glutamate (Sigma-Aldrich Cat# G6642; 1:500; RRID: AB_259946). Secondary antibodies used in the present study are as follows: Alexa Fluor 568 (Thermo Fisher A-11036 1:500; RRID: AB_10563566; Lot # 2155282).

Quantitative real-time polymerase chain reaction

Total RNA was extracted using TRIzol reagent, and cDNA was obtained by reverse transcription (Takara). The following primers were used: 5'-TCTACCCACCGCTCCACATT-3' (forward) and 5'-CCTGGCTCCCTGTCCCTTTCA-3' (reverse) for *Opn4*, 5'-AGGTCGGTG TGAACGGATTG-3' (forward) and 5'-TG TAGACCATGTAGTTGAGGTCA-3' (reverse) for *Gapdh*. Real-time qPCR was performed using the Light-Cycler 96 system (Roche) following the manufacturer's recommended protocols. Each reaction was performed in triplicate. A fragment of *Gapdh* was amplified as the internal control. Differences in gene expression were calculated by the $2^{-\Delta\Delta\text{CT}}$ method and are presented as the fold change.

Two-photon Ca^{2+} imaging

Surgery

1.5% isoflurane was used to induce anesthesia. Mice were rested on top of a heating pad to maintain body temperature at 37.5°C and ophthalmic ointment (Bepanthen, Bayer) was applied to both eyes to prevent damage from dehydration during surgery. After removing the scalp and the tissues over the skull, a custom-made black recording chamber was glued to the skull with cyanoacrylic glue (UHU, Buhl-Baden, Germany). The position of the primary visual cortex was located according to brain atlas coordinates. After a small craniotomy ($\sim 1.0 \times 1.0$ mm) was performed over the monocular region of left primary visual cortex, mouse was transferred into the set-up for subsequent dye stained. The recording chamber was perfused with warm (37°C) artificial cerebral spinal fluid containing (ACSF, 125 mM NaCl, 4.5 mM KCl, 26 mM NaHCO_3 , 1.25 mM NaH_2PO_4 , 2 mM CaCl_2 , 1 mM MgCl_2 and 20 mM glucose, pH = 7.4) bubbled with 95% O_2 and 5% CO_2 . In the experiments that cortical neurons were labeled with Cal-520 AM, mice were advanced to the dye stained step. In the experiments that cortical neurons were labeled with GCaMP6, mice were advanced directly to imaging step.

Dye stained

Primary visual cortex was stained *in vivo* with the fluorescent Ca^{2+} indicator dye Cal-520 AM⁷⁰ for multi-cell bolus loading. Cal-520 AM was dissolved in DMSO with 20% Pluronic F-127 for stock, and diluted with ACSF to a final concentration of 567 μM for bolus loading. Ca^{2+} imaging was performed ~ 1 h after dye injection, and the whole imaging lasted for up to 8 h.

Imaging

Around 1 h after dye injection or immediately after surgery, the level of anesthetic was decreased to 0.5% isoflurane for recordings, and the breathing rate of mice was kept 110–130 breaths/min by adjusting the concentration of isoflurane. *In vivo* Ca^{2+} imaging was performed by using a custom-built two-photon microscope system based on a 12-kHz resonant scanner (model "LotosScan 1.0", Suzhou Institute of Biomedical Engineering and Technology)⁶⁹ and a mode-locked Ti:Sa laser (model "Mai-Tai DeepSee", Spectra Physics) through a 40 \times /0.8 NA water-immersion objective (Nikon). Full-frame images at 600 \times 600 pixels were acquired at a 40-Hz frame rate by custom-programmed software written in LabVIEW.⁷¹ The typical size of the field-of-view was $\sim 200 \mu\text{m} \times 200 \mu\text{m}$. Multi-planes of imaging on average were acquired for each mouse.

Electrophysiology

In vitro perforated-patch recordings

Eyes were removed to the Ame's medium bubbled with 95% O_2 and 5% CO_2 immediately after mice were euthanized by high concentration of carbon dioxide. During recording, the retinal ganglion cell layer of was visualized under infrared differential interference (IR-DIC) optics at 940 nm. IpRGCs were identified by the virus expressed cre-dependent fluorescence marker before recording. For the melanopsin rescued experiments, retina was perfused with blockers cocktail to block the light inputs from rods/cones. For the

hM4Di experiments, retina was perfused with normal Ames's medium, and the fluorescence targeted ipRGCs were recorded before and after CNO application.

In vivo loose-patched recordings

Mice were kept anesthetized under 0.5% isoflurane. The dura was removed and the surface of brain was perfused by ACSF bubbled with 95% O₂ and 5% CO₂. Consecutive pressure was given to keep the tip of patch pipette clean during the penetration. The patch pipette formed a gigaohm seal with the targeted neurons.

In vivo multi-channel extracellular recording

A preparation surgery was performed 2 days prior to the in vivo multi-channel recording.⁷² Under the anesthesia, a metal post was mounted onto the skull of the mouse for head fixation with dental cement. A Teflon-coated silver was inserted into the other hemisphere as the reference channel. After the surgery, a silicon elastomer was applied to cover the surgical opening. Before recording sessions, the mouse was placed on a rotary disk and habituated for 1~2 h. During the recording, the silicon seal removed and a silicone electrode was then inserted into V1. Recording sessions were conducted at 5-6 different locations in V1 of each mouse. After all the recording sessions, Dil, a non-toxic fluorescent and lipophilic dye, was used to mark the recording sites. After all the recording sessions the mouse was euthanized to verify the recording location and viral expression. The signals were recorded by a 64-channel silicone probe (NeuroNexus) at 40 kHz sampling rate and then filtered with a bandpass filter (0.3-3 kHz) using OmniPlex Neural Recording Data Acquisition System (Plexon). To obtain single-unit spikes, we conducted a semiautomatic spike sorting using Offline Sorter (Plexon) and further analyzed the neuronal activity with customized MATLAB scripts, following previous studies.⁷²

Chemogenetic inhibition

CNO (Abcam, ab141704) were dissolved in phosphate buffer saline to a concentration of 1 mg/mL. During *in vivo* Ca²⁺ imaging, the intraperitoneal injection of CNO (10 μg/g) was performed after the 'Pre CNO' recording; the 'Post CNO' recording at the same focal plane was performed 30 min after the intraperitoneal injection of CNO. 10 μM CNO was applied for whole cell recording in hM4Di verification experiment.

Pupillary light reflex

Head-fixed mice were used for pupillary light reflex (PLR). All PLR experiments were performed during the day: from 3 h after light-on to 3 h before light-off with >1 h dark adaptation. To measure the diameter of pupil, an infrared CCD camera and a 470 nm LED (light intensity is 6×10^{14} photons/cm²/s.) were placed 1 cm in front of the cornea. Videos for contralateral eyes were recorded at a frame rate of 5 Hz and was analyzed with ImageJ software. The pupil area was measured at maximum constriction after light stimulation begin.

Visual stimulation for mouse model

Blue light stimuli

The blue light stimuli were delivered using a 470 nm LED and passed through a diffuser placed 10 mm from the right eye. Light intensity was adjusted smoothly through a custom-made adaptor, ranging from 7.35×10^{12} to 7.35×10^{16} photons/cm²/s. To generate a stable response to light with high intensity, each of trials was interleaved at least 5 min.

Sinusoidal gratings

Visual stimuli were generated by a computer and presented with a XENARC 700V LCD monitor (19.2 cm × 12.0 cm, 1280 × 800 pixels, 60 Hz refresh rate, 400 cd/m² maximum luminance) located 14 cm from eyes. Sinusoidal gratings were generated by a custom-GUI in Matlab (release 2012a; Mathworks Inc.) by using the Psychophysics Toolbox (<http://psychotoolbox.org/wikka.php?wakka=HomePage>), and were kept at 0.039 cycles per degree, 1 Hz and mean luminance 49.1 cd/m² in the imaging and behavioral experiment.⁷³ For the gratings in 100% contrast, the pixel values of luminance in the GUI were set to a range of 0 to 1, in which 0 stand for black and 1 for white. For measuring the gOSI and FWHM of V1 neurons, visual stimulus of a single trial starting with a black and a gray screen (with mean luminance, pixel values of luminance at 0.5) for 5 s, a following stationary grating for 2 s and the corresponding drifting grating for 2 s (full-field, 100% contrast, 1 Hz, 0.039 cycles per degree), were presented at 16 directions (separated by 22.5°) in a pseudo-random sequence. Evoked Ca²⁺ activity was imaged at least 6 trials at each focal plane. For the Ca²⁺ recording of *Opn4^{+/+};Opn4-Cre* mice expressing hM4Di or GFP, the same drifting gratings were represented at same visual field before and 30 min after CNO application. For the behavioral training, two types of interleaved drifting gratings with different orientations (100% contrast, 1 Hz, 0.039 cycles per degree, 4 s per trial) were presented in front of mice.

Blue-rich and blue-less gratings

We attenuated the inputs of three color channels (red, green and blue) individually in the MATLAB script to get a pair of gratings with different efficiency to activate ipRGCs but with the same mean luminance (41 cd/m²). We named the gratings with higher efficiency to activate ipRGCs as 'blue-rich' gratings, while another as 'blue-less' gratings. The other parameters of gratings were kept the same in the GUI.

Sinusoidal gratings mixed with visual noise

As control, sinusoidal grating with 30% contrast (pixel values of luminance ranging evenly from 0.35 to 0.65) was generated. A series of noise squares with different contrast (30%, 50% and 70%, pixel values evenly distributed in ranges = [-15, +15], [-25, +25],

[-35, +35] in %) were added onto the grating patterns pseudo-randomly, so that the grating patterns were increasingly blurred and invisible among the noise. Each pixel of the noise patterns was 4° in visual degree.⁷⁴

Locally sparse noise

To map the visual receptive fields (RF) of V1 neurons, we employed a “Locally Sparse Noise” stimuli basing on the visual stimuli developed in Allen Institute (https://observatory.brain-map.org/visualcoding/stimulus/locally_sparse_noise#). During the stimuli presentation, multiple black and white spots were presented in 100 ms and each spot was 5° on a side. Each spot was surrounded by a spatial exclusion region of 25° that was occupied by any other spot. At each location on the screen, white and black spots were presented 70 times randomly throughout the entire stimulus session.

Two-photon data analysis

Regions of interest (ROIs) and Ca²⁺ activity generation

To quantify the Ca²⁺ activity of individual neuron to stimuli, Labview scripts were used to manually draw regions of interest (ROIs) for cell bodies. The neuropil for each single ROI was defined as 2 μm further away from the border of the corresponding ROI. The contamination of neuropil were corrected by:

$$F = F_{ROI} - 0.7 * F_{neu}$$

where F_{ROI} is the transient fluorescence intensity within specified ROIs, and the F_{neu} is the transient fluorescence intensity of the corresponding neuropil. The Ca²⁺ activity was defined as follows:

$$\Delta F / F = (F - F_0) / F_0$$

where F_0 is the quarter site of fluorescence intensity from all pixels within specified ROIs during the last 1 s of gray screen presentation before the first stationary grating appears, or during the last 1 s of before 20 s blue light onset.

Response to 20 s blue light

The Ca²⁺ activity to 20 s blue light in MO mice V1 was defined as the integral of the $\Delta F / F$ over the stimulus period.

Response to drifting gratings

For each ROI in each trace, a Ca²⁺ transient can be defined as a signal only if its peak amplitude was greater than three times the standard deviation of the noise band of the trace. The noise band was the difference between the original trace and its smoothed trace, which was smoothed by exponential weighted average. All traces were carefully inspected after the automatic analysis. Neuronal response to gratings drifting at each direction was evaluated by the integral of the $\Delta F / F$ during the drifting window. Neurons were defined as responsive to drifting gratings when their response during at least one of the 16 directions was significantly higher than their activity during the black period at the traces start (ANOVA test).^{75,76}

Global orientation selectivity index

gOSIs were calculated to quantify the tuning level of individual neurons. A gOSI was defined as follows:^{77,78}

$$gOSI = \frac{\| \sum R(\theta) e^{2i\theta} \|}{\sum R(\theta)}$$

where θ is the direction of moving grating. $R(\theta)$ is the response to direction θ . $i = \sqrt{-1}$. gOSI ranges from 0 to 1. gOSI = 0 indicates that the neuron is unresponsive or responds equally to all orientations, while gOSI = 1 indicates the neuron responds exactly to just one orientation.

Full width of half maximum (FWHM)

We defined full width of half maximum (FWHM) to access the bandwidth of orientation tuning curve of each neuron. To quantify the FWHM, we fitted the neuronal responses to 16 directions drifting gratings as a function of orientation by the sum of two Gaussian functions with peaks 180° apart:⁴⁸

$$R(\theta) = a_0 + a_1 e^{-\frac{(\theta - \theta_0)^2}{2\delta^2}} + a_2 e^{-\frac{(\theta - \theta_0 - 180^\circ)^2}{2\delta^2}}$$

where $R(\theta)$ is the response at direction θ , a_0 is the untuned component of the response, a_1 and a_2 are the amplitudes of the two Gaussians, θ_0 is the fitted preferred-orientation and δ is the standard deviation of the Gaussian function. FWHM is measured by $2\sqrt{2 \ln(2)} * \delta$.

The fitting error was computed as:⁴⁸

$$E = \frac{\sum_{\theta} (R_{fit}(\theta) - R_{measure}(\theta))^2}{\sum_{\theta} (R_{fit}(\theta) - \bar{R})^2}$$

in which $R_{fit}(\theta)$ and $R_{measure}(\theta)$ are the fitted and measured responses at θ , respectively, and \bar{R} is the measured response averaged across all directions. We set a threshold of 0.5 for the fitting error; FWHM of a cell was included in the analysis only if the fitting error was below the threshold.

Cortical response variability

To quantify the response variability of each measured tuning curve, we computed the variance-to-mean:

$$V = \frac{\sum_{\theta} \text{VAR}(\theta)}{\sum_{\theta} R(\theta)}$$

in which $R(\theta)$ is the response at θ averaged across all trials, and $\text{VAR}(\theta)$ is the variance of the response at θ across trials. All of the analysis was performed in MATLAB.

Multi-channel recording data analysis

Receptive fields (RFs) mapping was conducted according to previous studies.⁷² ON and OFF RFs were determined based on the visually evoked responses to white and black spots, respectively. The evoked responses to the white or black spots at each location on the screen were averaged and a spatial map of evoked response Z-score can be obtained. Then, a 2D Gaussian filter was applied to the spatial maps to smooth the RF maps and RFs were defined as the area where the Z-score exceeded 3. To better characterize the shape of RFs, a 2D elliptical Gaussian function was used to fit the thresholded RFs in MATLAB, and the long and short axes were derived from the fitting results. The simple cell was identified based on an ON/OFF overlap index of less than 0.3.

The CANN models

The continuous attractor neural network

We adopt a continuous attractor neural network (CANN)⁷⁹ to model the representation of orientation in V1 L2/3 (Figure 4). In the CANN, excitatory neurons are aligned on a ring according to their preferred-orientations (θ), which are in the range of $(-\pi/2, +\pi/2]$ with the periodic boundary. Denote $u(\theta, t)$ the total synaptic currents at time t to neurons with orientation preference at θ , whose dynamics is written as,

$$\tau \frac{\partial u(\theta, t)}{\partial t} = -u(\theta, t) + \rho \int_{-\pi/2}^{\pi/2} J(\theta, \theta') r(\theta', t) d\theta' + I_{\text{ext}}(\theta, t) + \mu_b \xi_b(\theta, t), \quad (\text{Equation 1})$$

where τ denotes the time constant of the synaptic current, typically in the time order of 2~10 ms, ρ the neuronal density, ξ_b the background noise, i.e., Gaussian white noises of zero mean and unit variance, and μ_b the noise strength. In the simulation, since the number of neurons ($N = 1000$) in the CANN is limited, the integration term in Equation 1 is written as,

$$\rho \int_{-\pi/2}^{\pi/2} J(\theta, \theta') r(\theta', t) d\theta' = \frac{1}{N} \sum_{k=1}^N J(\theta, \theta^k) r(\theta^k, t). \quad (\text{Equation 2})$$

$J(\theta, \theta')$ is the synaptic connection strength between neurons at θ and θ' , which is set to be:

$$J(\theta, \theta') = J_0 \exp\left[-\frac{(\theta - \theta')^2}{2a^2}\right], \quad (\text{Equation 3})$$

where J_0 ($J_0 > 0$) controls the maximum connection strength and a the range of neuronal connection. Neurons have strong connections to their neighborhood and weak connections to distal neurons.

$r(\theta, t)$ is the firing rate of neurons with orientation preference at θ . The relationship between the synaptic current and the firing rate is given by:

$$r(\theta, t) = \frac{[u(\theta, t)]_+^2}{1 + k\rho \int [u(\theta, t)]_+^2 d\theta'}, \quad (\text{Equation 4})$$

where $[u]_+ \equiv \max(u, 0)$. The neuronal firing rate first increases with the input and then saturates gradually via divisive normalization by the total network activity, where the parameter k in Equation 4 controls the inhibition strength. Notably, in the CANN, we do not consider inhibitory neurons explicitly, but rather we model their effect by using the divisive normalization. In reality, divisive normalization can be achieved by shunting inhibition of inhibitory neurons.⁸⁰

In the CANN, the neuronal connection pattern is translation-invariant in the space of neuronal preferred-orientations, i.e., $J(\theta, \theta')$ is the function of $(\theta - \theta')$. Because of this symmetry, the CANN can hold a continuous family of localized bump states (in the limit of large N), with each of them encoding an orientation angle. When a visual stimulus orientated at θ_0 (denoted as $I_{\text{ext}}(\theta, t) = \alpha \exp[-(\theta - \theta_0)^2 / (2a^2)]$ with α controlling the input strength) is presented to the network, the bump response of the CANN is written as

$$\hat{r}(\theta, t) = r_{PO} \exp\left[-\frac{(\theta - \theta_0)^2}{2a^2}\right]. \quad (\text{Equation 5})$$

In our model, this bump state is interpreted as the neural population activity in response to a stimulus orientation θ_0 . It also represents the tuning curve of a single neuron when different orientation values are presented. Thus, r_{PO} is the amplitude of the tuning curve and a controls the tuning width. Therefore, we set $a = 0.4$ in Equations 1, 2, 3, and 4 according to the experimental data.

The condition for the CANN holding stationary bump states depends on the balance between the excitatory and inhibitory interactions in the network dynamics. The CANN falls into two different dynamical regimes (Figures S4C and S4D). i) when the inhibitory interactions between neurons are sufficiently strong (i.e., J_0 is very small or k is very large), the CANN can only hold the silent state ($r_{PO} \approx 0$) as its stationary state if there is no external input; ii) when the excitatory interactions between neurons are sufficiently strong (i.e., J_0 is very large or k is very small), in addition to the silent state, the CANN can hold a continuous family of active states ($r_{PO} \gg 0$) as its stationary states (attractors), even when external input is absent. These two dynamical regimes reflect two different strategies of network computation: the former corresponds to that the computation result is dominated by external inputs, while the latter the computation result is dominated by the internal dynamics of the network. In our case, the computationally appealing parameter values are at the boundary (denoted as k_c , $k_c = J_0 \rho / (8\sqrt{2\pi}a)$) between the above two dynamical regimes.⁷⁹ We find that when $k \approx k_c$, i.e., the bump state is marginally stable, the network response is most sensitive to the change of external inputs (Figures S4C and S4D), which is the parameter regime we use in the below study.

The external input signal to the CANN

We considered that the input signal to the CANN consists of two parts, which are from RGCs and ipRGCs, respectively, and denoted as $I_{RGC}(\theta, t)$ and $I_{ipRGC}(\theta, t)$, i.e.,

$$I_{ext}(\theta, t) = I_{RGC}(\theta, t) + I_{ipRGC}(\theta, t) + \mu_{ext} \xi_{ext}(\theta, t), \quad (\text{Equation 6})$$

where ξ_{ext} denotes Gaussian white noises of zero mean and unit variance, and μ_{ext} the noise strength.

Based on the experimental data (Figure 1), we set the visual input orientated at θ_0 induced by RGCs to be:

$$I_{RGC}(\theta, t) = \alpha_{RGC} \exp\left[-\frac{(\theta - \theta_0)^2}{2a^2}\right], \quad (\text{Equation 7})$$

This RGC input ensures that the tuning curves of V1 L2/3 neurons induced by RGCs (i.e., the bump state of the CANN induced by the RGC input) have the width as measured in the experiment. We do not consider the inhibitory input from RGCs, as their effect has been modelled by the divisive normalization in Equation 4.

For ipRGCs, we consider that they induce both excitatory and inhibitory inputs to the CANN, i.e., $I_{ipRGC}(\theta, t) = I_{ipRGC}^{Exc}(\theta, t) + I_{ipRGC}^{Inh}(\theta, t)$. Without loss of generality, we set the excitatory input induced by ipRGCs has the same form as that from RGCs, such that its effect is to increase the neuronal response amplitude as indicated by the experimental data. It is written as

$$I_{ipRGC}^{Exc}(\theta, t) = \alpha_{ipRGC}^{Exc} \exp\left[-\frac{(\theta - \theta_0)^2}{2a^2}\right], \quad (\text{Equation 8})$$

where α_{ipRGC}^{Exc} controls the strength of the excitatory input of ipRGCs.

For the inhibitory input to the CANN induced by ipRGCs, we set its form by fitting the experimental data (Figures 4F–4H), which gives,

$$I_{ipRGC}^{Inh}(\theta, t) = \alpha_{ipRGC}^{Inh} \exp\left[-\frac{(\theta - \theta_0)^2}{2a_{ipRGC}^2}\right], \quad (\text{Equation 9})$$

where α_{ipRGC}^{Inh} determines the input strength, and $a_{ipRGC} = 0.6$ determines the broadness of the input range.

Tuning curves of V1 L2/3 neurons modulated by ipRGCs

We investigated how the external input induced by ipRGCs affect the tuning curves of neurons in V1 L2/3. While fixing the strength of the input induced by RGCs to be a constant, i.e., $\alpha_{RGC} = 1.21$, we first inspected how the amplitude and the bandwidth of the tuning curve of a V1 L2/3 neuron are modulated by the input of ipRGCs under the condition of no noise (i.e., $\mu_b = \mu_{ext} = 0$).

The calculation details are as follows,

- (1) 36 different values of $\beta^{Exc} = \alpha_{ipRGC}^{Exc} / \alpha_{RGC}$ and $\beta^{Inh} = \alpha_{ipRGC}^{Inh} / \alpha_{RGC}$ equally spaced in the range of $[0.1 / \alpha_{RGC}, 1 / \alpha_{RGC}]$ were chosen, respectively.
- (2) With each parameter set of $(\beta^{Exc}, \beta^{Inh})$, external inputs orientated at $\theta_0 \in \{-90^\circ, -80^\circ, -70^\circ, -60^\circ, -50^\circ, -40^\circ, -30^\circ, -20^\circ, -10^\circ, 0^\circ, 10^\circ, 20^\circ, 30^\circ, 40^\circ, 50^\circ, 60^\circ, 70^\circ, 80^\circ\}$ were presented to the CANN trail by trail. Without loss of generality, we chose the neuron with preference at $\theta = 0^\circ$ as an example. We measured the firing rate of the neuron when each visual orientation stimulus was presented. Over trials, we obtained the tuning curve of the neuron.
- (3) With each parameter set of $(\beta^{Exc}, \beta^{Inh})$, we used the nonlinear least square method (Curve Fitting toolbox in MATLAB) to fit the tuning curve obtained in (2), and extracted the corresponding amplitude (denoted as $r_{\beta^{Exc}, \beta^{Inh}}$) and bandwidth (denoted as $\sigma_{\beta^{Exc}, \beta^{Inh}}$) of the tuning curve, respectively.
- (4) Similarly, we calculated the amplitude and the bandwidth of the tuning curve of the neuron without receiving the external input of ipRGCs, which are denoted as $r_{0,0}$ and $\sigma_{0,0}$, respectively.

(5) The modulation effects of ipRGCs on the amplitude and bandwidth of the tuning curve were measured by $(r_{\beta^{Exc}, \beta^{Inh}} - r_{0,0}) / r_{0,0}$ and $(\sigma_{\beta^{Exc}, \beta^{Inh}} - \sigma_{0,0}) / \sigma_{0,0}$, which are denoted as $\Delta r_{PO} / r_{PO}$ and $\Delta \sigma / \sigma$, respectively.

We found that (Figures S4E and S4F): (1) when $\beta^{Inh} \gg \beta^{Exc}$, both the amplitude and the bandwidth of the tuning curve decrease; (2) when $\beta^{Exc} \gg \beta^{Inh}$, the amplitude increases significantly while the bandwidth remains almost unchanged; (3) only when $\beta^{Exc} \sim \beta^{Inh}$, i.e., the excitatory and inhibitory inputs induced by ipRGCs are roughly balanced, the amplitude of the tuning curve increases ($\Delta r_{PO} / r_{PO} > 0$) while the bandwidth decreases ($\Delta \sigma / \sigma < 0$), which is consistent with the experimental finding.

To understand the underlying mechanism, we checked the ipRGC inputs $I_{ipRGC}^{Inh}(\theta, t)$ and $I_{ipRGC}^{Exc}(\theta, t)$ under the condition of $\beta^{Exc} \sim \beta^{Inh}$ (setting $\beta^{Exc} = 0.76/1.21$ and $\beta^{Inh} = 0.64/1.21$, the red colored circle in Figures S4E and S4F), and found that their superposition has a Mexican-hat shape (Figure 4J). Thus, the modulation effect of ipRGCs becomes clear. Consider a visual stimulus orientated at θ_0 is presented, and ipRGCs induce a Mexican-hat shaped nest input centered at θ_0 to the CANN. The neurons whose preferred-orientations close to θ_0 receive positive inputs from ipRGCs and their firing rates increase; whereas, the neurons whose preferred-orientations are very different from θ_0 receive inhibitory inputs from ipRGCs and their firing rates decrease. As the tuning curve measures how the firing rate of a neuron varies with different values of θ_0 , the overall effect of ipRGCs is to sharpen the tuning curve of a neuron in the CANN.

To be biologically more plausible, in addition to the input noises (controlled by μ_{ext} in Equation 6), we also consider heterogeneity in neuronal connections by including noises in the recurrent connections of the CANN, which is written as

$$J(\theta, \theta') = J_0 \exp \left[-\frac{(\theta - \theta')^2}{2a^2} \right] (1 + \mu_J \xi_J), \quad (\text{Equation 10})$$

where ξ_J denotes white gaussian noise of zero mean and unit variance and μ_J the noise strength.

With the consideration of several different noises (Equations 1, 6, 10), we first calculated the tuning curves of neurons when only the RGC input is presented. At each trial, we presented a visual stimulus orientated at θ_0 , with θ_0 taking one of 18 different values equally spaced in the range of $[-90^\circ, 90^\circ]$ to the CANN. We calculated the firing rate of the neuron trial by trial, and obtained the tuning curve of the neuron for 18 orientation values by averaging over 1000 times. Using the nonlinear least square method, we exacted the amplitude and bandwidth of the tuning curve, which give that the amplitude is 5.39 ± 3.93 and the tuning width is $43.64^\circ \pm 20.48^\circ$, and they are consistent with the experimental results.

We further calculated how the input of ipRGCs modulates the tuning curves of neurons with the consideration of noise. Following the same procedure as in the case of applying the RGC input only, we applied the inputs from both RGCs and ipRGCs to CANN, and measured the corresponding tuning curves. We found that: i) when only the excitatory input from ipRGCs is added to the network, it increases the amplitude of the tuning curve significantly, while the tuning width remains approximately unchanged; ii) when only the inhibitory input from ipRGCs is added to the network, it decreases both the amplitude and bandwidth of tuning curve; iii) when the roughly balanced excitatory and inhibitory inputs from ipRGCs are added to the network (i.e., $\beta^{Exc} \sim \beta^{Inh}$, the red colored dot in Figures S4E and S4F), the amplitude of the tuning curve increases, and meanwhile the bandwidth of the tuning curve decreases (Figures 4K and 4L). Specifically, the bandwidth of the tuning curve is $39.52^\circ \pm 21.76^\circ$, which decreases 9.44 % from the value $43.64^\circ \pm 20.48^\circ$ when only the input from RGCs is considered; the amplitude of the tuning curve increases 30.8% to the value 7.05 ± 5.2 when only the input from RGCs is considered. Our results are consistent with the experimental findings shown in Figure 1 in the main text.

The Methods for Computing the Tuning Curves of Neurons with noise are as follows: (1) For a fixed parameter $(\alpha_{ipRGC}^{Exc}, \alpha_{ipRGC}^{Inh})$, external inputs orientated at $\theta_0 \in \{-90^\circ, -80^\circ, -70^\circ, -60^\circ, -50^\circ, -40^\circ, -30^\circ, -20^\circ, -10^\circ, 0^\circ, 10^\circ, 20^\circ, 30^\circ, 40^\circ, 50^\circ, 60^\circ, 70^\circ, 80^\circ\}$ were presented to the CANN trial by trial. We measured the firing rate of a neuron when each visual orientation stimulus was presented. Over 18 trials, we obtained the tuning curve of the neuron, and exacted the amplitude and bandwidth of the tuning curve by using the nonlinear least square method (Curve Fitting toolbox in MATLAB). (2) We randomly generated 10 different copies of the CANN according to Equation 10 (corresponding to different animals). For each network, we repeated the computation in (1) for 100 times, and got 100 values of the amplitude and the bandwidth for each neuron. (3) By averaging the results in (2), we got the statistical results about the amplitude and bandwidth of neurons.

Decoding orientation representation from V1 L2/3 neural population response with the visual noise

The population vector method was utilized to decode orientation representations of visual stimuli based on the recorded population activity of V1 neurons in different mice. The computation is as follows:

(1) For the i th neuron recorded under a visual noise condition ($\tilde{\beta} = 0$), its preferred orientation ($\theta_i^{\rho, \tilde{\beta}}$) is calculated by,

$$\theta_i^{\rho, \tilde{\beta}} = \sum_{k=1}^K \frac{\bar{x}_k^{\tilde{\beta}}(i, k) \rightarrow}{Z} \theta_k,$$

where $\bar{x}^{\beta}(i, k)$ denotes the mean activity of the i th neuron when the visual stimulus is θ_k and the noise strength $\tilde{\beta} = 0$ (for $k = 1, \dots, K$, with $K = 8$ the number of visual stimuli, $Z = \sum_{k=1}^K \bar{x}^{\beta=0}(i, k)$, and $\theta_k \in \{-\pi, -3\pi/8, -\pi/4, -\pi/8, 0, \pi/8, \pi/4, 3\pi/8\}$). Statistical analysis shows that the preferred orientations of V1 neurons in both *Opn4^{+/+}* and *Opn4^{-/-}* mice are almost uniformly distributed, ensuring unbiased decoding outcomes by the population vector method.

- (2) The population vector method was employed to decode the neural representation of the presented visual orientation (θ_m^{β}) in the m th trial with the noise strength β . The decoding result $\theta_m^{\beta, \text{decoded}}$ is given by,

$$\theta_m^{\beta, \text{decoded}} = \sum_{i=1}^N \frac{x^{\beta}(i, m)}{Z} \vec{\theta}_i^{\beta, \tilde{\beta}=0},$$

where $x^{\beta}(i, m)$ represents the activity of the i th neuron in the m th trial, for $i = 1, \dots, N$, and $m = 1, \dots, M$, with N the number of V1 neurons recorded in the experiments and M the number of experimental trials, and $\beta = 0, 0.3, 0.5, 0.7$. Note that the population vector estimates the orientation by calculating the weighted average of neurons' preferred directions with the weights given by the responses of neurons in the trail. $Z = \sum_{i=1}^N x^{\beta}(i, m)$ is the normalization factor.

- (3) The accuracy of representation in the m th trial is quantified by $\rho_m^{\beta, \text{bias}} = |\theta_m^{\beta, \text{decoded}} - \theta_m^{\beta}|$.
- (4) To ensure an equitable comparison between *Opn4^{+/+}* and *Opn4^{-/-}* mice, despite the variability in neuron counts, we sampled identical numbers of neurons ($N = 223$) and trails of population activities ($M = 40$) from each mouse in each run, and the accuracy of representation in each mouse is averaged over 20 different runs with randomly sampled neurons. The statistical accuracies of representation (denoted as $P^{\beta, \text{bias}}$) are calculated with 3 *Opn4^{+/+}* and *Opn4^{-/-}* mice, respectively.

Our results indicated that i) at the same noise strength, *Opn4^{+/+}* mice consistently outperformed *Opn4^{-/-}* mice in representational accuracy, with statistical significance; ii) the difference of discrimination biases between *Opn4^{+/+}* and *Opn4^{-/-}* mice are larger when stimuli were interfered with external noise (Figures 5N–5S). This result indicates that cortical inputs from ipRGCs enhance the V1 resilience to external visual noise.

All the simulation parameters used in the CANN modal are shown in Table S1.

Mouse behavioral experiment

In brief, we first trained mice to learn an easy Go/No-Go task containing gratings with 60° or 45° orientation difference. Mice that successfully learned the easy task were then advanced to multiple testing tasks containing gratings with smaller orientation differences for measuring the orientation discriminability. In experiments for assessing resilience to visual noise interference, mice were advanced to multiple $\Delta 30^\circ$ tasks that contain gratings mixed with noise of different contrast.

Head-plate implant

Adult mice (2–4 months) were anesthetized by 1.5%–2.0% isoflurane. Ophthalmic ointment (Bepanthen, Bayer) was applied to both eyes to prevent damage from dehydration during surgery. Dental acrylic (Super Bond C&B) was used to fix the head plate onto the skull after removing the scalp and tissues. Mice were transferred to a heating pad for awake. Mice were prepared for experiment after 2 days' recovery.

Perceptual discrimination task

Mice were water-deprived 2 days before training start. The body weights of mice were recorded every day. The weight was maintained from 70% to 85% to keep both the health of the mice and their motivation to lick the water tube. During training, the mouse was head-fixed and stayed in an acrylic tube within a sound and light-proof box. Tongue licks were detected by an iron tube connected with a custom-made capacitive sensor.⁸¹ Training ended when the mouse stopped licking for several minutes. The entire behavioral experiment contained four phases: habituation, conditioning, easy discrimination, hard discrimination.⁸²

Habituation step

The habituation step typically last 2 days. Mice were head-fixed at the training instrument and given $\sim 4 \mu\text{L}$ water for each lick.

Conditioning step

The conditioning step typically last 2 days. Mice were trained to lick for water rewards in response to a vertically oriented gratings drifting rightward (Go cue). Each visual stimulation drifting for 4 s, and mice licking during the last 2 s of the visual stimulation (response window) was rewarded with $\sim 4 \mu\text{L}$ of water (hit). If no lick was detected during the response window (miss), water reward would also be given at the end of the visual stimulus. When the number of hits reached 150 within 30 min, the mouse was advanced to the next step.

Training step

For training step, gratings in 100% contrast with 60° and 45° orientation difference to vertically oriented gratings (No-Go cue) were added into the training to form $\Delta 60^\circ$ and 45° tasks. Mice licking within the response window of Go trials was rewarded with water, whereas licking within the response window of No-Go trials was punished with a mild air puff (200 ms) and a longer inter-trial interval (6 s, timeout). Mice were neither rewarded nor punished for no licking within the response window of Go (miss) and No-Go

(CR, correct reject) trials. Each session was divided into multiple blocks containing 20 trials, and the $\Delta\theta$ between Go and No-Go cue in each block was fixed. Blocks with $\Delta 60^\circ$ and 45° orientation difference were alternated. The Go and No-Go trials were randomly interleaved, but the same stimulus was never repeated more than 3 times. The performance of mice measured discriminability (d'), which was quantified by:

$$d' = \text{norminv}(\text{hit rate}) - \text{norminv}(\text{FA rate}),$$

where norminv is the inverse of the cumulative normal function.⁴⁸ Hit rate = number of hits / number of Go trials, and FA rate = number of FAs / number of No-Go trials. Higher d' values indicate better performance in visual discrimination.

Mice were trained 2 sessions per day. After reaching a stable performance for at least 5 sessions, mice were advanced to testing step. Mice failed to reach the threshold ($d' \geq 1$) within 20 sessions were abandoned from experiment.

In the experiments mixed with visual noise, mice were trained in task $\Delta 30^\circ$ with gratings in 30% contrast.

Testing step

For testing step, we introduced another 6 hard tasks ($\Delta 30^\circ$, $\Delta 25^\circ$, $\Delta 20^\circ$, $\Delta 15^\circ$, $\Delta 12^\circ$ and $\Delta 10^\circ$, Figure 5C) into the Go/No-Go experiment. Each Blocks with different $\Delta\theta$ were presented randomly. The testing step generally last one day. To eliminate the trials when the mouse was satiated or distracted from the task, we only included the blocks with $> 70\%$ hit rate.

After finished the testing step, d' of 8 different $\Delta\theta$ task were fitted by Hyperbolic function to get the discriminability curve for each mouse. The threshold stands for the minimum $\Delta\theta$ mouse could discriminate ($d' = 1$). Mice were then advanced to $\Delta 10^\circ$ task with gratings in blue-rich and blue-less spectra.

For the melanopsin rescue experiment, mice above were intravitreally injected with AAV2/2-hSyn-DIO-mOpn4-EGFP or AAV2/2-EF1 α -DIO-GFP. Three weeks later, mice were retrained by $\Delta 60^\circ$ and 45° tasks. After reaching their performance at training step, we again applied testing step to mice to get their d' at different $\Delta\theta$ tasks. Estimation of threshold of orientation discrimination after intravitreal injection was as the same as above.

In the experiments mixed with visual noise, we only performed task $\Delta 30^\circ$. As control, sinusoidal grating with 30% contrast (pixel values ranging evenly from 0.25 to 0.75, with 0 means black and 1 white, respectively) was generated. A series of noise squares with different contrast (30%, 50% and 70%, pixel values evenly distributed in ranges = [-0.15, +0.15], [-0.25, +0.25], [-0.35, 0.35]) were added onto the grating patterns pseudo-randomly.

Procedure for human visual orientation discrimination

In brief, we first constructed a display to independently manipulate the effective radiance to activate ipRGCs (step 1), and then applied it to individually validate the 'metameric' spectral pair for the generation of three testing spectra with different effective radiance to activate ipRGCs but the same to each type of cones (step 2 and 3). After that, we tested the orientation discrimination threshold for each subject by presenting gratings of the same contrast but generated from each of three testing spectra (step 4).

Step 1: Visual stimuli of human psychophysical experiment

We used two projectors (model PA500U; NEC, Japan, 1920 × 1200 pixels, refresh rate of 60 Hz) to generate a composite 4-primary image onto a projection screen for all human psychophysical experiments (Figures 6A and S6A).⁵² We modified the output of two projectors by inserting optical filters into the light path of channels of each projector. In one of the projector, the blue channel was modified by a 450 nm band pass filter (bandwidth 25 nm) to make a 'violet' primary; and the green channel was modified by a 550 nm band pass filter (bandwidth 25 nm) to produce a narrower 'green' primary. The output of the red channel was attenuated by inserting a neutral density filter into the light path to make a 'red' primary. In the other projector, the blue channel was modified by a 485 nm band pass filter (bandwidth 25 nm) to make a 'cyan' primary; and the output of green and red channels were blocked by 450 nm band pass filters (bandwidth 25 nm). All the filters used above were custom-made by Anhui Institute of Optics and Fine Mechanics, Chinese Academy of Sciences. By superimposing the output of these two projectors onto a projection screen, we achieved a four-primary display.

The projected image of the projectors was displayed at an area of 59 × 93 cm covering 23° × 36° visual angle at a viewing distance of 146 cm (Figure 6B). A spectral radiance colorimeter (SRC-200S, EVERFINE Corporation, China) was used to calibrate the output of the projector channels individually. The stimuli were generated and controlled by MATLAB (R2012b; The MathWorks Inc., Natick, MA, USA) and Psychophysics Toolbox extensions.

Participants were seated in front of the projection screen in a dark room and were asked to fixate their left eye (right eye were covered with an eye patch) on a fixation dot on the screen (Figure 6B). A chin and head rest was used to minimize head movements and to maintain a fixed viewing distance. Gaze position and pupil size of the left eye were monitored by an eye-tracker (EyeLink 1000, SR Research Ltd., Ottawa, Ontario, Canada) during experiments.

Stimuli were all circular sinusoidal gratings (15° diameter) presented at 20° retinal eccentricity (19° temporal and 6.5° superior to the fixation dot). The edges of gratings were smoothed with a Gaussian kernel with a standard deviation of 1.5°.

Step 2: Receptor silent substitution and metamerism

To specifically stimulate ipRGCs, the method of receptor silent substitution and metamerism^{83,84} was used to generate a spectral pair which is functionally indistinguishable for cones but contained significant contrast for ipRGCs (Figure S6B).⁵² Such spectral pair is called 'metameric' pair and consists of a 'reference' spectrum with lower effective radiance to activate ipRGCs and a 'melanopic' spectrum with higher effective radiance to activate ipRGCs. Using the Silent Substitution Toolbox⁸⁵ in MATLAB, we got the

published CIE 2006 spectral sensitivity of L, M and S cones⁸⁶ for 10° visual field and generated melanopsin sensitivity using a template (called nomogram) with peak at 480 nm (Figure 6A).⁸⁷ Pre-receptor filtering was corrected for L, M and S cones. Then we employed the published spectral sensitivity of L, M, S cones and ipRGCs⁸⁶ in a theoretical ‘standard observer’ to calculate a standard spectral pair for the four channels that would produce spectral outputs that had equivalent effective radiance to activate cones but differed in effective radiance to activate ipRGCs (theoretical standard ‘metameric’ pair). The theoretical standard ‘metameric’ pair consist of a ‘reference’ spectrum with low effective radiance to activate ipRGCs (melanopic radiance = 0.11 W/m²/sr), and a ‘melanopic’ spectrum with high effective radiance to activate ipRGCs (melanopic radiance = 0.16 W/m²/sr). The luminance of reference spectrum was 113 cd/m² and CIE 1931 xy chromaticity was [0.31, 0.33]. However, considering the inter-individual variations in cone spectral sensitivity and/or pre-receptor filtering, such standard ‘metameric’ pair may not be suitable for each subject. We therefore generated 169 variants of these pairs for each subject by making small alterations to the spectral composition of the melanopic spectrum in the standard ‘metameric’ pair while keeping the reference spectrum unchanged (Figure 6C).

Step 3: Validation of ‘metameric’ pair

Spatial frequency testing protocol. Since ipRGCs could discriminate pattern at low but not high spatial frequency,⁵² the criterion for the spatial frequency of gratings we used to validate individual ‘metameric’ pair in the following online-tuning section is to find the spatial frequency that well within the sensitivity range of cones but beyond the sensitivity range of ipRGCs for each subject. To this purpose, we first presented grayscale gratings that have radiance contrast to all photoreceptors at variant spatial frequencies. Stationary sinusoidal gratings were randomly presented in one of four orientations (0°, 45°, 90° or 135°) at one of six spatial frequencies (0.2, 0.4, 0.8, 1.6, 3.2, 6.4 cycles/degree) and at one of three contrasts in grayscale (Michelson contrast = 0.06, 0.11 or 0.2). The background spectrum equaled to the ‘melanopic’ spectrum. Stimuli were presented until a participant reported its orientation by keypress, with an inter-stimulus interval of 2 s. Each stimulus was presented ten times. The correct rate for orientation discrimination at each spatial frequency was calculated as the average correct rate to stimuli at the three contrast levels and then plotted as a function of spatial frequency. The highest spatial frequency that can be distinguished by cones for individuals was defined as the spatial frequency with 90% correct rate by linear interpolation and was used in online-tuning step to identify specific ‘metameric’ pair. Prior to each experiment, a practice session was conducted to help subjects be familiarized with the task procedure.

Online-tuning protocol. The online-tuning step aims to individually validate the specific ‘metameric’ pair for each subject. Considering the inter-individual variations, we generated 169 variants of standard ‘metameric’ pair by slightly alternating the melanopic spectrum, while the reference spectrum was consistent. For each pair, the grating stimulus was generated by mixing the ‘reference’ and ‘melanopic’ spectra alternately into a sinusoid pattern and the background spectrum was the mean of ‘reference’ and ‘melanopic’ spectra (Figure 6C). Gratings mixed by different pairs were pseudorandomly presented in one of four orientations at a fixed spatial frequency (with 90% correct rate in the spatial frequency test, generally above 3.2 cycles/degree) well within the sensitivity range of cones but beyond the sensitivity range of melanopsin, and participants were then asked to report which of four orientations were presented. Each stimulus was presented until a participant reported the orientation, and then the stimulus was replaced by a homogenous background for an inter-stimulus interval of 2 s. Each stimulus was presented twice, but if the stimuli were incorrectly recognized at least one time, it would be presented for a third time. For each participant, spectral pairs incorrectly recognized 3/3 times were collected into the pool of potential ‘metameric’ pairs. These potential ‘metameric’ pairs would be checked again for another 4-time test (the procedure was identical to the online-tuning test) for each participant. The spectral pair with correct rate at 25% (chance level) or lower was consider as validated ‘metameric’ pair and was used for orientation discrimination testing individually.

Spatial frequency tuning protocol of melanopsin. This step aims to further confirm that the validated ‘metameric’ pair for each subject is indistinguishable to L, M and S cones but visible to melanopsin. The spatial frequency sensitivity for melanopsin was tested using the same method as the spatial frequency test above (measuring the spatial frequency sensitivity for all photoreceptors and melanopsin), but using the stimulus generated by the validated ‘metameric’ spectral pair instead of grayscale spectrum. Spectral pairs with different effective radiance to melanopsin (low = 0.12, middle = 0.14, high = 0.16 w/m²/sr) was achieved by mixing the validated ‘metameric’ pair at different ratio (Figure 6D). For spectral pair with each effective radiance to melanopsin, the grating stimulus was generated by mixing the spectral pair alternately into a sinusoid pattern, while the background spectrum was the mean of the spectral pair. The mean percentage of correction at each spatial frequency was calculated and then compared with the spatial frequency sensitivity of grayscale stimuli (Figure S6D).

Step 4: Orientation discrimination testing protocol

Orientation discrimination ability were tested with three background spectra of different melanopic radiance (low = 0.12, middle = 0.14, high = 0.16 W/m²/sr) which were generated by proportionally mixing the validated ‘metameric’ pair (Figure 6D). The order of these three conditions was counterbalanced among subjects (Figure S6E). A single trial consisted of two successively displayed sinusoidal gratings (SF = 0.2 cycles/degree, Michelson contrast = 0.46) with different orientations (rotated $\pm \Delta \theta$ to a vertical grating). Gratings were presented for 250 ms, with an interval of blank for 500 ms, and then the participants were asked to report whether the second grating was rotated clockwise or anticlockwise to the first grating (Figure S6E). Three-up-one-down staircase procedure was

used to measure the discrimination threshold which maintains an accuracy at 79.4%.⁸⁸ When the staircase reversals reached 12 times, the testing experiment finished and the threshold of orientation discrimination for each participant was calculated by averaging the last 10 reversals.

QUANTIFICATION AND STATISTICAL ANALYSIS

Data analysis and statistics were performed using LabVIEW and MATLAB. For all experiments, Wilcoxon rank-sum test, signed-rank test, Kolmogorov-Smirnov test, two-way ANOVA or Kruskal-Wallis followed by multiple comparison tests were used (* $p < 0.05$, ** $p < 0.01$, *** $p < 0.001$; n.s., no significant difference).